UNIVERSITY OF CALIFORNIA
RIVERSIDE

Phase Resolved Optical Coherence Tomography for Label-Free Detection of Neural Activity

A Dissertation submitted in partial satisfaction
of the requirements for the degree of

Doctor of Philosophy

in

Neuroscience

by

Minh Quang Tong

December 2018

Dissertation Committee:
Dr. B. Hyle Park, Co-Chairperson
Dr. Michael E Adams, Co-Chairperson
Dr. Hongdian Yang

The Dissertation of Minh Quang Tong is approved:

_____

_____

Committee Co-Chairperson

_____

Committee Co-Chairperson

University of California, Riverside

ACKNOWLEDGEMENTS

Thank you, Dr. B. Hyle Park, for your patience and guidance during that last four years. Your patience is of a saint. You were able to handle all my mistakes, even those that resulted in the failure of an entire optical system. Your guidance is of a light house. You were there to provided valuable suggestions but also allowed me to explore new ideas. All this work would not be possible without your support. I wish your family the best!

I would also like to thank my dissertation committee members, Dr. Michael Adams and Dr. Hongdian Yang, for their time to review my project through the years and providing valuable feedback. Dr. Michael Adams has been knowledgeable and supportive through my entire graduate school life, without him I would be lost, thank you so much. In addition, I would like to thank my oral qualifying committee members, Dr. Devin K. Binder and Dr. Xiaoping Hu for reviewing my proposal and guiding me to achieve it.

I would have become insane and lonely if it were not for the support of my lab mates. I would like to thank Dr. Rezuanul Haque for being a mentor when I first rotated in the lab during the summer. Thank you, Christian Oh, for being a great friend and mentor while I was still learning how to align the 800 system. Thank you, Dr. Koji Hirota for your continued support even after your graduation but most importantly for being a great friend. Thank you, Dr. Monirul Hasan for not only being a great friend but struggling with me as we aligned the 800 system for tomorrow's experiment or going out for curry. Thank you, Jorge Sanchez for being a friend and keeping me company while I was aligning the OCT system or programming. I owe you some Taco Bell. Thank you, Jason Qiu for your

friendship and for putting up with my “Minh” jokes. Thank you, Dr. Michael C. Oliveira, Dr. Carissa Rodriguez, Danielle Ornelas, Christopher Lee Hughes, Junze Liu, Jasmine Shah, and Patrick Gregory for your support on all the different projects. All of you are amazing people. I would also like to thank the neuroscience and bioengineering communities.

I would like to acknowledge the funding sources that contributed to the work, which includes the NIH R00 EB007241, NIH R01 NS081243, CAL-BRAIN 349329, NIH R21 EY026441, NIH U01 EY025501, and the CNAS deportment for allowing me to be a teaching assistance.

Lastly, I would like to thank my family for supporting me throughout my Ph.D. journey and beyond. Thank you, Ba and Mẹ for your support. Thank you, Linh, Tam, and Brian for being amazing siblings.

Minh Tong

Riverside, California

To my family
For their lifelong dedication, love, care and support

ABSTRACT OF THE DISSERTATION

Phase Resolved Optical Coherence Tomography for Label-Free Detection of Neural Activity

by

Minh Quang Tong

Doctor of Philosophy, Graduate Program in Neuroscience
University of California, Riverside, December 2018
Dr. B. Hyle Park, Co-Chairperson
Dr. Michael E Adams, Co-Chairperson

Current methods for detection of nervous system activity have been limited to electrophysiology, which requires the electrode to contact the nervous system or optical-based techniques that require incorporation of reporter agents. Both methods are golden standards but have limitations. Optical coherence tomography (OCT) is an imaging technique based on light that measures intrinsic structural changes associated with an action potential. A benefit of using OCT is that it does not require any exogenous agents and is minimally invasive. Phase-resolved OCT detects 1-30 nm swelling of an axon during neural activity. In my studies described here, phase-resolved OCT was used to detect the swelling *Drosophila* neurons when presented with ecdysis triggering hormone as well as a 1-3 nm swelling of a cockroach axon caused by action. However, since phase imaging is limited to one point, the dissertation ends with development of the line field swept source OCT system that can provide images of a b-line or cross-sectional image without using a scanning device.

Table of Contents

List of Figures

Introduction

The act of decision making is done by an assembly of neurons that make up the nervous system. The nervous system acts as a control center for our entire body by processing all external and internal stimuli, retaining and recalling memory, and maintaining regulatory systems. Each individual neuron can generate, or relay electrical signals based on the flow of ions across the plasma membrane, resulting in coordination, dissemination, and acquisition of information. Our nervous system makes us who we are, enabling us to perceive the beauty of life so that we could teach our children and remember loved ones. Therefore, understanding the dynamic mechanism of the nervous system would help develop new treatments for neurological disorders. Current techniques for measuring neural activity, such as electrophysiology, provide excellent electrical readings, but lack high resolution and are invasive. In addition, many of these techniques lack depth information.

Shank electrodes yield depth information; however, they have a limited resolution and a fixed geometry. Multi-electrode arrays produce stable and reliable 2D information, but they are not applicable to all experiments. Fluorescence imaging yields high specificity along with, temporal and spatial resolution, but requires the introduction of a fluorophore into the region of interest either genetically or mechanically. However, the introduction of such fluorophores can lead to cellular toxicity and genetically-encoded fluorescence is not available for all model organisms. Thus, my research aim is to detect neural activity using optical coherence tomography (OCT). However, to verify the presence of neuronal activity,

electrophysiology and fluorescence imaging are used as golden standards for the comparison of optical signals from OCT. These optical signals result from intrinsic structural changes that accompany neural activity and the goal is to eventually have a technique that is label-free and able to detect localized action potentials.

This dissertation is organized into five chapters. Chapter 1 introduces the concept of OCT as well as its potential use in neuroscience. In short, the chapter explains the principle and mathematical representation of OCT, SD-OCT, and phase-resolved OCT. The chapter also discusses some application and potential in neuroimaging.

Chapter 2 discusses the design, development, and characterization of the spectral domain OCT system. This chapter calculates the physical resolution and field of view axially and laterally. It also calculates the signal to noise ratio (SNR) off of a mirror and phantom as well as determines the phase noise.

Chapter 3 measures the optical phase changes from the central nervous system (CNS) of the *Drosophila*. The OCT beam is positioned over a neuron while the CNS is presented with a hormone to trigger neural circuitry underlying innate ecdysis behavior. The beam is fixed at one location of the neuron to reduce lateral phase noise. Calcium mobilization in subsets of neurons involved in ecdysis circuitry is monitored via cell-specific expression of the calcium fluorescence indicator GCaMP.

Chapter 4 focuses on the cockroach nerve cord to associate optical neural activity data with electrical activity. Active neurons swell, displacing the neurons surrounding them

that may not have been active, thus modifying the optical data as observed in Chapter 3. A nerve cord consists of multiple nerve fiber. In this chapter, I describe the use of electrical stimulation to trigger action potentials from giant axons within the nerve cord of the cockroach while recording electrical and optical phenomenal for a one-to-one comparison. Thickness changes of cockroach axons registered by OCT were closely associated with action potentials temporally.

Chapter 5 addresses concerns regarding lateral movement by building a line field swept-source OCT system. This system is capable of imaging a cross-sectional image without lateral scanning, thus avoiding lateral motion noise. Without lateral phase noise the limiting factor is the signal to noise ratio. The system is capable of imaging structural images using intensity and will require more alignment to capture reasonable phase images.

The dissertation concludes with a summary of the overall findings of this study and highlights the significant achievements that can motivate future research studies.

Chapter 1: Introduction of Optical Coherence Tomography

1.1. Optical coherence tomography (OCT)

Optical Coherence Tomography (OCT) was demonstrated in 1991 by David Huang in James Fujimoto's group[1]. They demonstrated how this optical imaging modality was able to capture high resolution, cross-sectional images from biological tissue microstructures by measuring the magnitude and echo time delay of backscattered light similar to ultrasound [1, 2]. This chapter will show the basic principles of the OCT system as well as a brief description of similar modalities used for neuronal imaging and recording.

1.2.Principle of OCT

The imaging technique best compared to OCT is ultrasound imaging. For ultrasound imaging, a sound pulse is sent and the reflection (echo) is measured to create an image, whereas in OCT, light echoes are measured by a Michelson interferometer, using the low coherence properties of a broadband light source. Light weaves travel too quickly to be directly measured through reflected pulses as is used in ultrasound. Thus, by using the two different arms of the Michelson interferometer and adjusting the two lengths of the arms an interference fringe pattern is created[3]. By measuring the interference patterns, the location and strength of the reflections can be determined. The first OCT system to apply this approach was called time domain OCT (TD-OCT). An alternative approach to TD-OCT is Fourier domain OCT (FD-OCT). Fourier domain OCT includes two types of

detection methods, spectral domain OCT and swept source OCT, which will be explored in more detail in this chapter.

1.2.1.Fourier Domain OCT

OCT is a powerful imaging technique using coherent light to capture micrometer resolution images by measuring the magnitude and echo time delay of backscattered light. OCT is based on low-coherence interferometry. Different types of low-coherence interferometry methods are used to study biological tissue invasively and non-invasively[2, 4-6]. Under conventional interferometry with long coherence lengths, interference of light occurs over distances of meters. In OCT, the interference is shortened due to the broad-bandwidth light source. This low-coherence length is advantageous when applied via a Michelson interferometer (see Fig.1.1).

In TD-OCT the depth profile of a sample is acquired by moving the reference arm along its length to map out the sample's reflectivity as a function of axial depth. An alternative method of acquiring a depth profile is through the measurement of a multitude of wavelengths separately, called Fourier Domain OCT (FD-OCT). Imaging in the Fourier domain can be done in two ways, by using a spectrometer which is named spectral domain OCT (SD-OCT) or by using a rapidly tunable laser named swept source OCT (SS-OCT). Both detection methods are used within this research. For a single wavelength that is captured by these systems, the reflectivity of a sampler is determined by the periodicity of

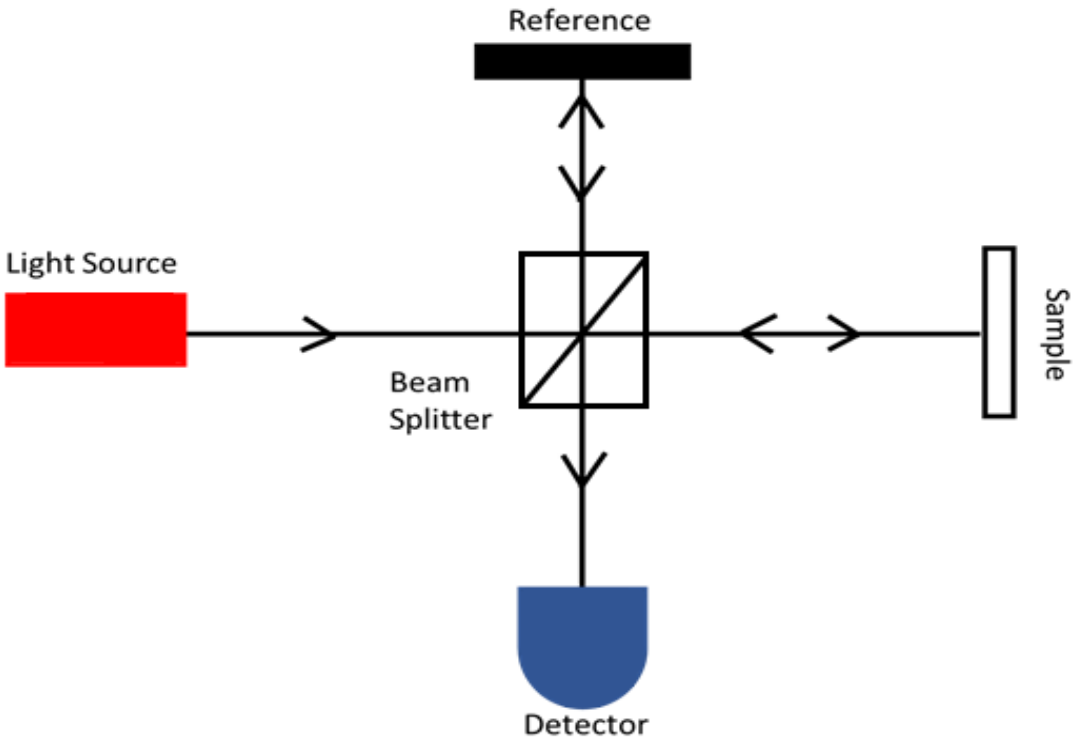

Figure 1.1 The Michelson interferometer consists of 4 arms. The light source sends light onto the beam splitter, from which it is sent to a sample and reference arm. Reflected light from both arms recombines to create an interference, pattern at the detector.

the refractive index modulation along the beam. This single wavelength along the beam provides information on the strength of the periodic refractive index modulation with a periodicity determined by the wavenumber $k = \frac{2\pi}{\lambda}$. λ is the wavelength. By combining information of the multiple wavelengths, a depth profile is created by a Fourier transformation of the reflectivity as a function of wavenumber.

Of the two implementations of FD-OCT. It uses a broad band light source and a spectrometer whereas the growing SS-OCT measures wavelength dependent reflectivity with a single balance detector and a light source that has a narrow band of light that is rapidly tuned over a large optical bandwidth. Both systems use the Michelson interferometer system as seen in Fig.1. A Michelson interferometer is used to measure the interferometric modulation of the output intensity that is detected by the photodetector when reference and sample arm delays are nearly matched[1]. The range of interference between the sample and reference arm is referred to as the coherence gate. The detector output is demodulated to yield an envelope of the interferometric signal, which is then digitized and stored in the computer. These detected interference patterns are used to extract information to produce the structural image of the sample.

It was not apparent that SD-OCT had certain advantages over TD-OCT until 2003, when de Boer et al. reported that there was a SNR gain of several hundredfold in SD-OCT over TD-OCT. Further studies reported that the sensitivity advantage of SD-OCT over TD OCT was between 20 to 30 dB[7]. With more improvements the gap between the two systems became larger and the sensitivity advantage over TD-OCT was more than 80 dB,

even in low light[9]. There are two important differences between TD-OCT and SD-OCT: first, the reference arm of TD-OCT is continuously moving while SD-OCT remains stationary, and second, the interference patterns are dispersed by diffraction grating before being detected by charged couple device (CCD). A typical SD-OCT is shown in Figure 1.2. The light is sent through a fiber beam splitter, where it splits the light between the reference and sample arms. The sample arm consists of a scanning mirror, which controls the scanning pattern of light. The backscattered light from the reference and sample arm recombined in the fiber to make interference patterns. The detector arm has a diffraction grating, which splits the light by wavelength. Finally, a focusing lens is used to focus the light onto the line scan camera.

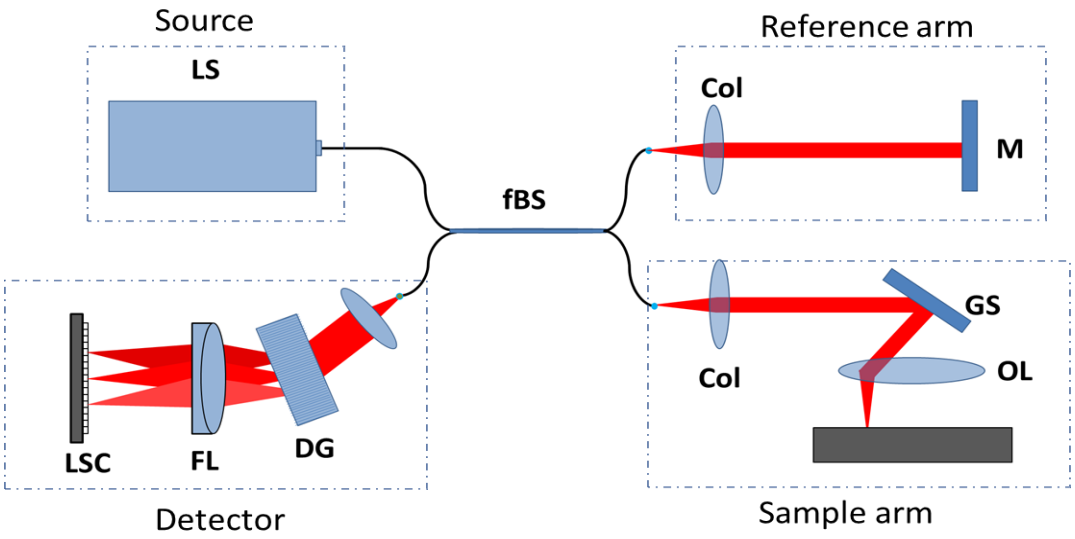

Figure 1.2 Schematic diagram of SD-OCT system. LS: light source, M: mirror, GS: galvo scanner, Col: collimator, OL: objective lens, DG: Diffraction grating, FL: focusing lens, LSC: line scan camera

The Michelson interferometer measures the field of light rather than its intensity. The incident light is divided into sample beam E_S and reference beam E_R. The electric field

at the output of the interferometer is the sum of the sample and reference fields, $E_S + E_R$, and the detector measures the intensity of the output. The intensity, I_D at the detector can be expressed as[10]:

$$I_D(k,\omega) = \frac{\rho}{2}\langle|E_S + E_R|\rangle^2 \tag{1.1}$$

where ρ represents detector sensitivity, k is the wavenumber ($\frac{2\pi}{\lambda}$) and ω is the angular frequency ($2\pi\upsilon$). Here, λ is the wavelength of the light and υ is the frequency of the light. If the polychromatic plane wave is used as a source for illumination, then the incident beam's electric field can be expressed as $E_i = s(k,\omega)e^{i(kz-\omega t)}$. Here, $s(k,\omega)$ is the amplitude of electric field while the $e^{i(kz-\omega t)}$ term expresses the phase of the light.

The intensity at the detector as a function of wavenumber can be further expressed into 3 parts: DC term, interference, and the autocorrelation noise. The can be expressed as the following:

$$\begin{aligned} I_D(k) = \frac{\rho}{4}[S(k)(R_R + R_{S1} + R_{S2} + \cdots \ldots)] \\ + \frac{\rho}{2}\left[S(k)\sum_{n=1}^{N}\sqrt{R_R R_{Sn}}\,(\cos[2k(z_R - z_{Sn})])\right] \\ + \frac{\rho}{2}\left[S(k)\sum_{n\neq m=1}^{N}\sqrt{R_{Sn}R_{Sm}}\,(\cos[2k(z_{Sn} - z_{Sm})])\right] \end{aligned} \tag{1.3}$$

The first part of the equation (1.3) is independent of the path difference between reference and sample arm referred as "DC terms". The middle part depends on source wavenumber and pathlength difference between sample and reference arm for each sample

reflector. This is the most important part, defined as “Cross-correlation terms”, and is proportional to square root of sample reflectivity. The third term represents the interference between different sample reflectors referred to as “autocorrelation”.

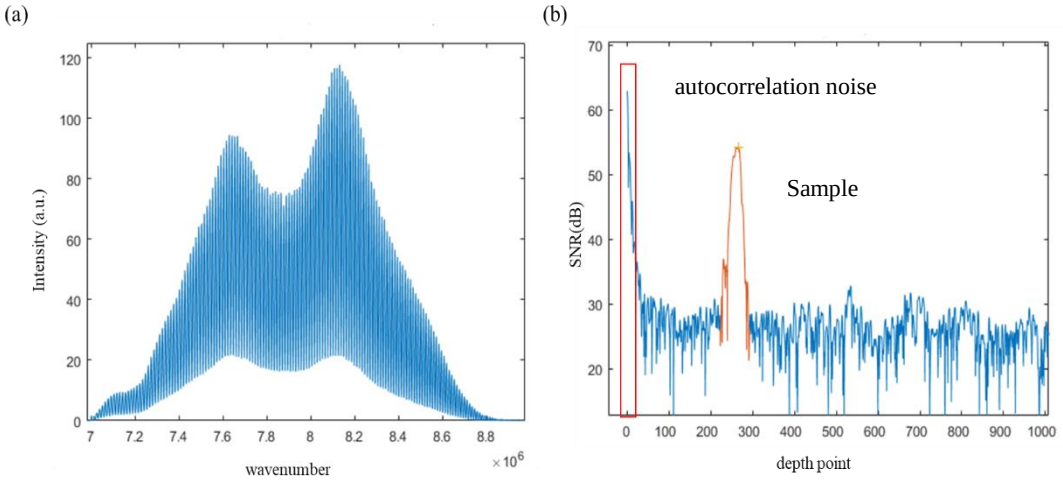

Figure 1.3 Detected spectrum and depth profile from a mirror. (a) detected wavenumber varying spectrum from line scan camera. (b) depth profile. The red box shows the autocorrelation noise at the top of the image.

In SD-OCT, all spectral components of $I_D(k)$ are captured simultaneously by a detector array. Inverse Fourier Transform of $I_D(k)$ provides the sample reflectivity profile. Figure 1.4b shows the A-scan (depth profile) of a mirror. This depth profile was generated by removing the DC part from the spectrum. The top red box is the auto-correlation noise terms of the image and the mirror is in between depth point 250 and 300.

The interferences seen in fig.1a create the image of a mirror seem in fig.1b. However, the sharpness of resolution of the is affected by several things within the optical systems from the sample to the laser. Thus, it is important calculate the parameters of an OCT systems from the theoretical values. These parameters may include the axial and lateral resolution, imaging depth, and field of view. The axial resolution of the system, assuming the source is a gaussian spectrum, is given by[1]:

$$\delta_z = \frac{2\ln(2)}{\pi}\frac{\lambda_0^2}{\Delta\lambda} \tag{1.2}$$

The λ_0 is the central wavelength and $\Delta\lambda$ is the bandwidth. The axial resolution depends solely on laser properties. For example, a laser with a central wavelength of 804 nm and bandwidth of 170 nm, would have an axial resolution of 1.67 μm using the equation above. The lateral resolution is dependent on the diffraction limited spot size of the focused beam. It should be noted that the diffraction limited minimum spot size is inversely proportional to the numerical aperture (NA) of the beam. Thus, a 40x objective would have a smaller spot size then a 10x objective. The lateral resolution can be defined in two ways[11]:

$$\delta_x = \frac{4\lambda}{\pi}\frac{f}{d} \tag{1.2}$$

where d is the spot size of the beam of the objective lens and f is the focal length of the NA. Notice that there is no direct connection between axial and lateral resolution. However, the lateral resolution is inversely related to axial field of view(FOV) or imaging depth range. The axial FOV can be expressed by two times the Rayleigh range of a gaussian

beam. The axial field of view can then be defined in relation to the lateral resolution of the Rayleigh range:

$$FOV_{axial} = \frac{\pi \Delta x^2}{\lambda} = \frac{0.565\lambda}{sin^2[\frac{\sin^{-1} NA}{2}]} \tag{1.3}$$

There is a tradeoff between lateral resolution and depth of penetration. Thus, increasing the lateral resolution will decrease the depth of penetration. The lateral FOV is dependent upon the lateral scanning system employed. This usually means the movement of the sample arm beam through the lens is dependent upon the scanning angle which determines the lateral FOV.

1.2.2.Phase-resolved OCT

Spectral information yields structural details in the microlevel while, phase information can detect transient changes in the nanometer level. The phase can be calculated as:

$$\varphi(z) = tan^{-1}(\frac{Im[i_D(z)]}{re[i_D(z)]}) \tag{1.4}$$

This phase can be utilized to detect small thickness change in the sample. The phase has common mode noise which can be eliminated by subtracting phase from two reflecting points, (one point is the reference point at position, z_{ref}, another point is the desired point, z_n). The phase difference at any time, t, can be calculated as:

$$\Delta\varphi(z_n) = \varphi(z_n) - \varphi(z_{ref}) \tag{1.5}$$

where depth point, n=1, 2, and so on.

Common mode noise can be eliminated without reference point by subtracting the phase of two depth points at time t,

$$\Delta\varphi(z_n) = \varphi(z_n) - \varphi(z_{n-1}) \tag{1.6}$$

The phase difference can be converted to path difference. If a wave is moving along the x-axis, then it changes by a phase of 2π for path changes of λ (Figure 1.5a).

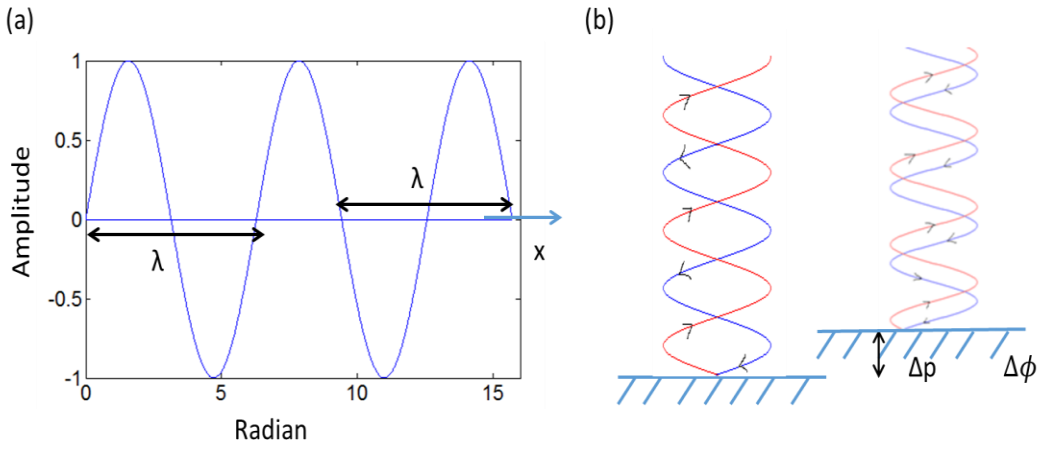

Figure 1.4 Relation between phase difference and path difference. (a) A wave changes phase of 2π after passing a distance equal to its wavelength, λ. (b) for a phase difference of Δϕ, light beam crosses a path difference of 2Δp for the OCT system

For phase-resolved OCT, light reaches a depth position of a sample, and returns, i.e. it crosses the path length twice for a phase difference (Figure 1.b). Hence, path difference or the thickness change of a sample can be calculated as:

$$\Delta p = \frac{\lambda}{4\pi}\Delta\varphi \tag{1.7}$$

The fundamental limitation of detection of minimum thickness change arises from signal-to-noise ratio (SNR) of a measurement. For a shot noise limited system, noise can be modeled as a random vector, and the minimum detectable phase difference[12, 13] is given by:

$$\sigma_{\Delta\varphi} = \frac{1}{\sqrt{SNR}} \tag{1.8}$$

The smallest meaningful phase difference $\Delta\phi = \phi(z_1, t) - \phi(z_2, t)$ can then be estimated by the standard deviation of the phase difference between the points, and can be expressed by:

$$\sigma_{\Delta\varphi} = \sqrt{\frac{1}{2SNR(z_1,t)} + \frac{1}{2SNR(z_2,t)}} \tag{1.9}$$

Let the acquired SNR and phase be denoted by $SNR(z, t)$ and $\phi(z, t)$, where z represents the depth within a single depth profile acquired at time t. Hence, the higher the SNR of a system the more sensitive it must be to detect smaller thickness changes.

A series of measurements from the front and back surfaces of a coverslip with a variable neutral density filter was acquired, and standard deviation of the phase differences was then calculated. A composite value for the SNR from the front and back surfaces was calculated by equating Eq. (1.9) to the more commonly used expression for phase noise of

$\sigma_{\Delta\phi} = \sqrt{1/SNR}$, which assumes the same SNR between both locations, to instead yield an expression that allows for improved assessment of the mean SNR versus phase for points with different SNR,

$$\sigma_{\Delta\varphi} = \sqrt{\frac{1}{2SNR(z_1,t)} + \frac{1}{2SNR(z_2,t)}} \tag{1.9}$$

A scatterplot of the composite SNR versus the phase noise is shown in Fig. 1.6 and demonstrates excellent agreement between experimental values and theoretical expectation.

1.3. Applications of OCT

OCT has been used in many different fields of research in many various fields such as ophthalmology[14-34], neuroimaging[35, 36], cardiology[19, 37-41], dental imaging[42-47], dermatology[16, 48-51], developmental biology[52, 53], tissue engineering[54-57], nanodevices[29, 53, 58], materials[59-63] etc. OCT has been used as a point scanning-based imaging system but can also acquire cross-sectional imaging by scanning in other direction to give 2D or 3D imaging. It can also acquire real time imaging from tissue[16, 64-68]. OCT has many potential applications where real-time imaging is required. Due to OCT's potential for high rate real time imaging it is a great tool to explore various neural studies.

1.4. OCT in neuroscience

There is a need in neuroscience for a non-invasive imaging modality that can detect a single spike while exhibiting a behavior. This need has driven development of many new imaging modalities each with pros and cons. Current fluorescence microscopy techniques [24, 69-72], fMRI[73-77], CT-scan[78], to PET-scan[79-81], althoughexcellent at detecting neural activity, they lack spatial resolution and require dyes. Other than fluorescence microscopy, electrophysiology is the gold standard for detection of neural activity; however, it is inherently invasive and lacks spatial resolution[82-87].

It should be noted that other optical imaging techniques, including diffuse optical tomography(DOT)[55, 88, 89], intrinsic optical imaging (IOS) [33, 49, 90, 91], photoacoustic tomography and microscopy[53, 92], and spatial frequency domain imaging(SFDI) [93, 94] have high resolution and are minimally invasive. Optical coherence tomography is a non-invasive imaging technique capable of, acquiring 3D volumetric images. OCT can detect neural activity by quantifying changes of backscattered light intensity [95-98]and phase[18, 99-103]. It is a promising tool for investigation of neural activity of the brain *in vitro* [104-107].

1.5.Conclusion

OCT detects optical changes either from scattering or absorption down to the micrometer scale, while using phase allows detection oft changes at the nanometer scale. First-generation TD-OCT used a moving reference arm, while the second-generation SD-OCT had a stationary reference arm with a spectrometer. OCT is utilized to diagnose different diseases, especially in ophthalmology, cardiology, and dermatology to name a few. It is also used for detection of neural activity in both *in vitro* and *in vivo* animal models.

Chapter 2: Combining optical coherence tomography with electrophysiology and fluorescence

2.1. Introduction

Current methods for detecting neural activity range from optical imaging to using magnetic resonance imaging[75-77, 79, 80, 108-110], calcium imaging[111] and voltage sensitive dye imaging[112-114]. However, these methods generally are either highly invasive, limited in depth, and indirectly monitoring secondary signals like blood oxygenation/flow. However, current optical imaging techniques such as diffuse optical tomography (DOT)[55, 88, 115] and intrinsic optical signal (IOS)[116-118] overcome these limitations and can detect relatively intense neuronal activity such as seizures through monitoring changes of intrinsic optical properties.

This chapter describes the configuration of SD-OCT, SS-OCT, and combined SD-OCT and fluorescence systems. OCT is a label-free, non-contact imaging technique that acquires depth-resolved images[117-120] with a point scan or a line scan. The basic principle of each OCT system follows the Michelson interferometer, which captures the interference between the reference arm and sample arm. When both sample and reference arm are within the coherence gate, backscattered light from various depths in a sample create this interference, thus producing an image. OCT is a promising technique for *in vitro*[55, 111] and *in vivo*[111, 119] imaging in highly scattering tissues. This chapter will also demonstrate the method used to calibrate and characterize each system for detecting changes in optical properties of biological tissue during neural activity.

2.2. System development

2.2.1. Spectral domain optical coherence tomography (SD OCT)

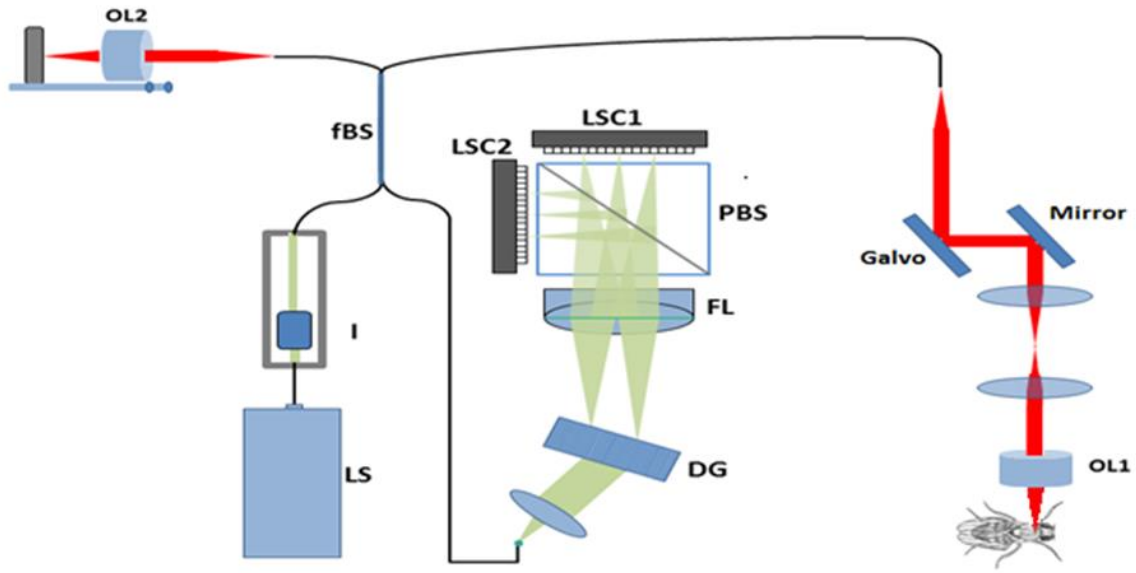

Figure 2.1 Schematic of combined spectral domain optical coherence tomography (SD-OCT) and fluorescence microscopy system. LS: light source (Ti:Sapph 800nm laser), I: isolator, fBS: fiber-based beam splitter, PBS: plate beam splitter, OL2: 20X objective lens (N.A 0.4), OL1: 20X water immersion objective lens (N.A. 0.50) DG: diffraction grating, FL: focusing lens, PBS: polarization beam splitter, LSC: line scan camera.

Figure 2.1 shows a schematic diagram of the 804nm OCT system. The system uses a Ti:Saph broadband mode locked laser (Femtolasers, Inc., Integral OCT 2709) with a center wavelength of 804nm and a bandwidth of 170nm. The laser light from the source is contained within a 2x2 wideband fiber optic coupler for lasers at a center wavelength of 805nm. The coupler splits the light as a ratio of 75:25. Seventy-five percent of the light will travel to the reference arm collimator while twenty-five percent of the remaining light will travel to the sample arm collimator. Using this configuration more reflected light will return from the sample arm.

Within the sample arm a galvanometer-based 2-axis optical scanner from Cambridge Technology, model 6210H, is used for raster scanning across the sample. The other part of the light exits into the reference arm that includes several dispersion-compensating blocks from Thorlabs to match the sample arm glass path length and to compensate for the dispersion between the two arms. The reference arm also includes a 20x objective with an N.A of 0.5, while the sample arm uses an Olympus UMPlanFl 20x/0.50 N.A water immersion objective. The light is reflected from both arms and recombined once they reach the coupler. The coupler collects the combined light, which travels to the spectrometer. The spectrometer consists of a diffraction grating (DG) from Wasatch Photonics with 12001pmm centered at 830nm, a focusing lens from Thorlabs with a focal length (FL) of 100mm, and a one-line scan camera from Basler Sprint, model number sp4096-140km. The detected spectrum in the camera are sent to the computer through a frame grader from National Instruments, model number NI1429. The second acquisition card, also from National Instruments, model number NI6259, is used to run two BNC breakout boxes (BNC 2110 and 2120). These two BNC breakout boxes generate the control trigger for the OCT line scan camera and scanning mirrors. The maximum acquisition speed of the OCT line scan camera is 144000 lines/seconds and yields a temporal resolution of the order of 7μs.

2.2.2.Fluorescence microscopy (FM)

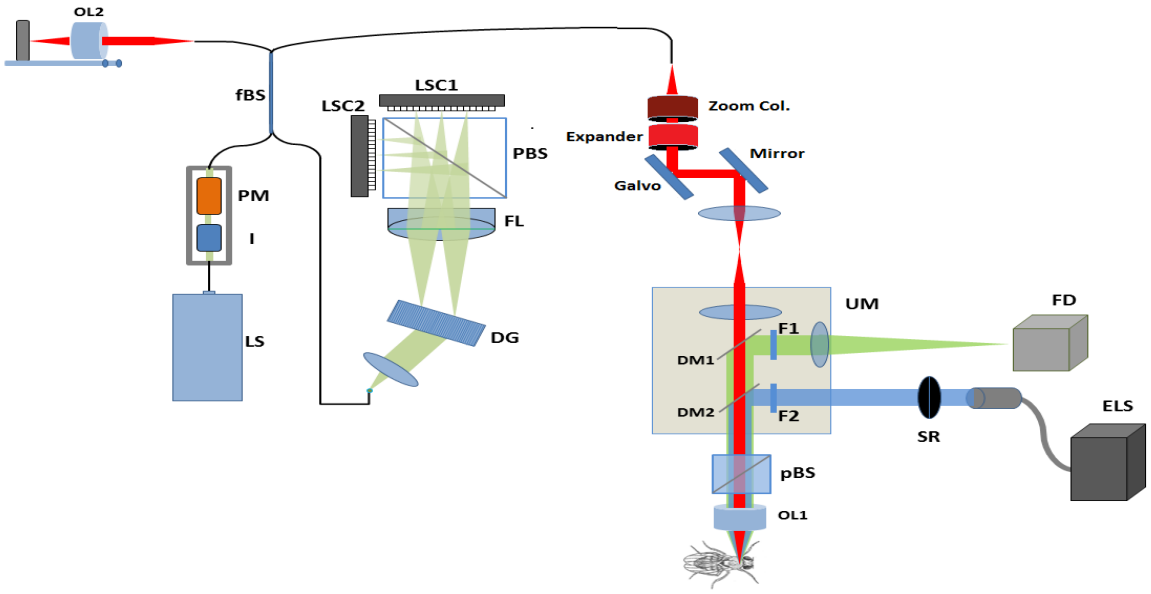

Figure 2.2 Schematic of combined spectral domain optical coherence tomography (SD-OCT) and fluorescence microscopy system. LS: light source (Ti:Sapph 800nm laser), I: isolator, PM: polarization modulator, fBS: fiber-based beam splitter, M: mirror, UM: upright microscope, PBS: plate beam splitter, OL2: 20X objective lens (N.A 0.4), OL1: 20X water immersion objective lens (N.A. 0.50) DG: diffraction grating, FL: focusing lens, PBS: polarization beam splitter, LSC: line scan camera, S: moving stage, F: filter, FD: Fluorescence detector (CCD), ELS: fluorescence excitation light source, SR: Shutter

Figure 2.2 shows a schematic diagram of the 804nm OCT system combined with fluorescence microscopy. Fluorescence microscopy used in these experiments provide high-resolution images of calcium dynamic corresponding to neural activity. In addition, it will provide contrast between the background and the fluorophore. This contrast is achieved using fluorophores such as GCaMP[120] and Arclight[121]. By simultaneously recording fluorescence and OCT signals, I attempt to correlate neural activity with neuronal swelling.

The fluorescence system uses a Lambda XL (Sutter Instrument) as its excitation light source which has a spectra range of 300 to 700nm. The light exposure time is controlled using

a stimulation shutter. After the light passes through the shutter and enters the microscope, it is combined with the OCT light. In the upright microscope, the excitation dichroic mirror (DM2) filters the light to allow 488 wave lengths (with a broadband range of 35nm) to pass and reach the 20x objective where it is focused on to the sample. The excitation light is absorbed by the sample, which then emits light as a response. The emission light returns to the microscope and passes through the excitation dichroic mirror until it reaches the emission dichroic mirror (DM1), where it is directed towards the high gain Electron Multiplier-CCD camera (Hamamatsu: C9100-02). Both the fluorescence stimulation shutter and the fluorescence CCD are controlled by a signal generated from the same BNC breakout box (BNC 2110 and 2120). The OCT trigger is synchronized with the breakout box; thus, synchronizing both systems. The information detected by the fluorescence CCD camera is sent to the computer through the frame grabber (Active Silicon). The CCD camera has a field of view (FOV) of 450μm X450μm and has 1000 X 1000 pixels. The CCD camera can also acquire images at the maximum rate of 16.7 frames/s. The acquisition can be accelerated up to 242 frames/s with 16 x 16 binning options.

2.3.System characterization

2.3.1.Characterization of OCT systems

The resolution, imaging range, and processing speed are some characterizations that will determine whether a device will be used for a given experiment. When a system is being described one of the first things mentioned is the resolution. One such resolution is the spatial resolution. For an OCT system there is the axial and lateral resolution. The theoretical lateral resolution of an SDOCT system is primarily determined by the final

imaging lens or an objective as well as the central wavelength. The lateral resolution (δ_x) can be expressed as[122]:

$$\delta_x = 0.37\frac{\lambda_0}{Sin(\alpha)} = 0.37\frac{\lambda_0}{NA} \quad (2.3)$$

Where the numerical aperture is shown as NA = sin(α), assuming the back aperture is filled. In our case the back aperture is not filled, for the equation that our system would use look at equation 1.2. This was because the NA would limit the axial field of view. Before discussing the field of view, spatial resolution should be mentioned. The axial(δ_z) resolution can be expressed in equation 1.1 [122, 123]. Note that the spectrum measured at the detector may differ between the source and what is detected by the detector. Also, the coherence length is the same as the axial resolution. This is due to the response of optical components and the detector itself.

The imaging depth of an OCT system. The axial field of view is propositionally linked to the NA and is given in equation 1.3. This term defines the full width at half maximum power of the confocal axial response function as the axial FOV of the OCT system. The lateral field of view for an OCT system depends greatly upon the lateral scanning of the system. A scanning system employs a means of rotating the beam inn the sample arm through the input aperture of the objective lens to maximum one-side scan angle θ_{max}. The lateral FOV can be expressed as:

$$FOV_{lateral} = 2f\theta_{max} \quad (2.2)$$

Where f is th focal length of the numerical aperture of the objective lens and θ_{max} is the maximum scan angle.

All these values are the theoretical resolution which was also partially discussed in chapter 1. However, the physical or realistic resolution is usually worse than the theoretical because the optical parts in the lens are not perfect. In practice, the last imaging lens or in our chance the microscope objective and the central wavelength of the light source are never perfect. The optical component within the OCT system introduces chromatic aberration. This aberration creates the effect of dispersion. Dispersion causes the failure for the lens to focus all wavelengths to the same convergence or focus point. This is corrected by using an achromatic doublet. Another issue is the reflection off the lens, this is corrected by using anti-reflectivity coatings that are spectrally dependent on the wavelength. However, this does not completely solve the issues and therefore the lateral resolution still degrades away from the focal plane due to defocusing and aberration. The maximum depth $z_{RD} = \lambda^2/4\Delta\lambda$ where $\Delta\lambda$ is the wavelength spacing between pixels, and $w = \delta\lambda/\Delta\lambda$ where $\delta\lambda$ is the spectrometer's spectral resolution. Note that the axial resolution is not affected by the optical lens in the system. To determine the physical axial resolution mirror information is collection and its full width half max (FWHM) is determined. That value multiplied the theoretical number is the axial resolution.

Another important characterization that defines a system is the SNR on a mirror or from a tissue sample. An example of measuring the SNR from the spectrometer is the use of an optical phantoms[124]. Optical phantoms are used to mimic tissue and give reliable SNR before imaging tissue instead of using a mirror for measuring the SNR. Figure 2.3

shows an experiment where a tissue-mimicking optical phantom with microspheres were used to measure the SNR and resolution at random depths. In figure 2.3a the *en face* image of the optical phantom shows many microspheres throughout the sample. Figure 2.3b shows the cross-sectional image of the same sample and figure 2.3c is the depth profile of a similar cross-section of a single microsphere. The amplitude of the largest peak of the depth profile minus the noise floor is the SNR.

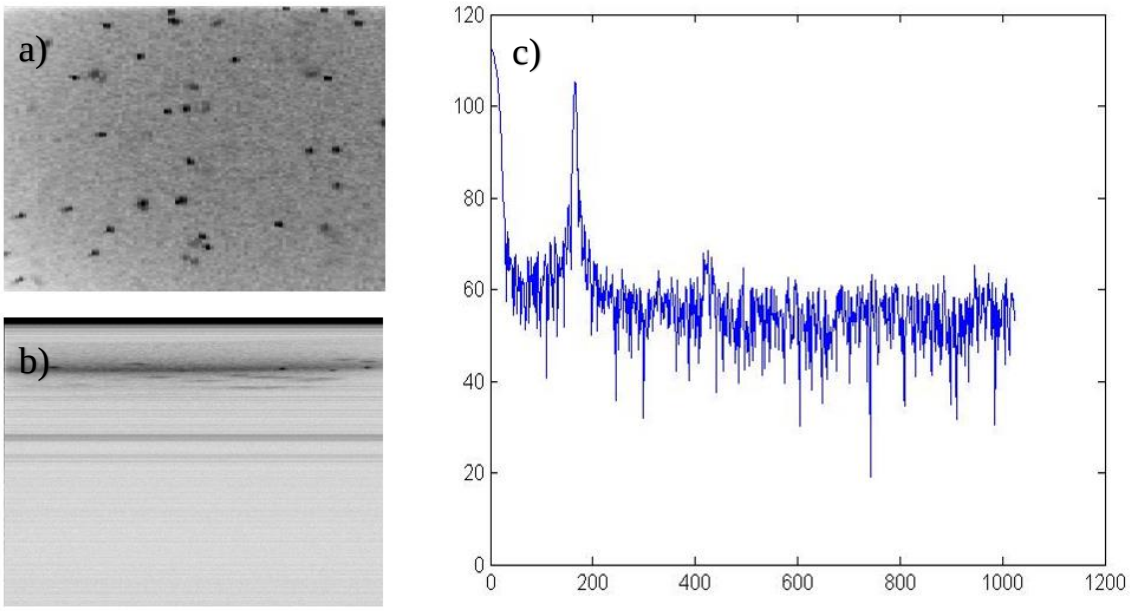

Figure 2.3 (a) *en face* image of an optical phantom with microspheres while in (b) the image is of the cross-section. (c) Depth profile of a single cross-section

Using the phantom as described provides information on the amount of light returning. However, it is also important to know the phase sensitivity. Using a coverslip for characterization the SNR can be changed or the amount of light in the sample arm is attenuated with a neutral density filter vs the phase difference between two surfaces would give the phase sensitivity of the system as shown in Figure 2.4 [103]. A composite value

for the SNR from the front and back surfaces was calculated by equating Eq.1.9 to the more commonly used expression for phase noise of $\Delta\phi_\sigma = \sqrt{1/\mathrm{SNR}}$. This equation assumes the same SNR from both locations, to instead give an expression that allows for improved assessment of the mean SNR versus phase for points with different SNR.

$$\mathrm{SNR} = \frac{2\sin(z_1, t)\,\sin(z_2, t)}{\sin(z_1, t) + \sin(z_1, t)} \tag{2.3}$$

Note that the higher the SNR the phase noise is lower, and the system can detect smaller intrinsic changes down to the nanometer level. The standard deviation of figure 2.4

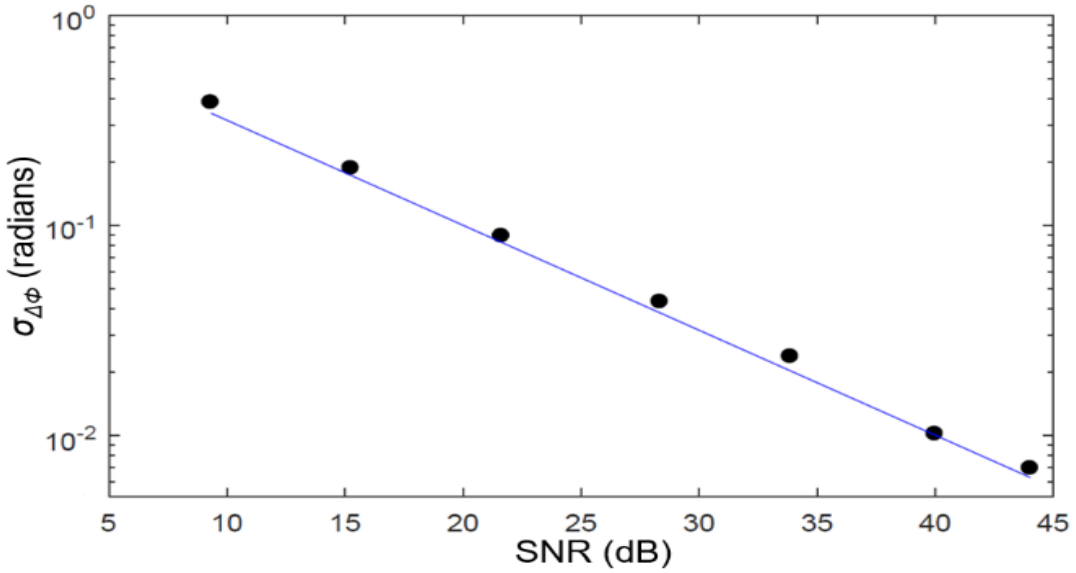

Figure 2.4 Measurements of the standard deviation of the phase difference between the front and back surfaces of a coverslip at various settings of a neutral density filter. The standard deviations are plotted using the composite SNR expression given in Eq. 2.1. The line indicates the SNR-limited phase noise floor.

2.3.2.Fluorescence characterization, data acquisition, and processing

Similar to OCT, fluorescence microscopy requires characterization to determine whether the system is ready to image. These parameters include the lateral resolution and

the alignment of the CCD FOV to the OCT lateral FOV. Both information can be collected by imaging an USAF-1951 air force target. The lateral resolution is taken from one cross-sectional line of the USAF-1951 air force target at the focus where there is both mirror and glass surfaces within the imaging line. Using that cross-sectional line, the values from the glass surface and mirror surfaces will differ. The lateral resolution can then be described as how will can the camera clearly depict the transition from glass to mirror. Thus, to determine the lateral resolution the plot of these traditional locations is required. Taking one cross-sectional line it is divided into two parts. The first part will include the first pixel number to the end subtracted by one. The second part will include the second pixel to the end. By subtracting these two parts together it will yield the transitional areas between the edges of glass and mirror as curves. By examining one of the curve's FWHM the lateral resolution can be determined.

Using the same USAF-1951 air force target, however, now instead of a cross-sectional line the whole image is used so that the FOV can be measured. USAF-1951 air force Group 6, Element 1is used for spatially register between the OCT and fluorescence systems (Fig. 2.5). The lateral scanning was restricted to 150 x 100μm as there was a visible loss of OCT sensitivity when the lateral scan exceeded this range. Several common features were identified from both the brightfield and OCT en face images. These features were used to determine cross-correlation parameters (scaling factor and rotation angle) between pixels of the OCT and brightfield images to align and match the images. The resulting images show a close overlap between a red overlay of OCT data with a blue overlay from

the fluorescence system shown in Fig. 2.5 demonstrates spatial registration of the two systems.

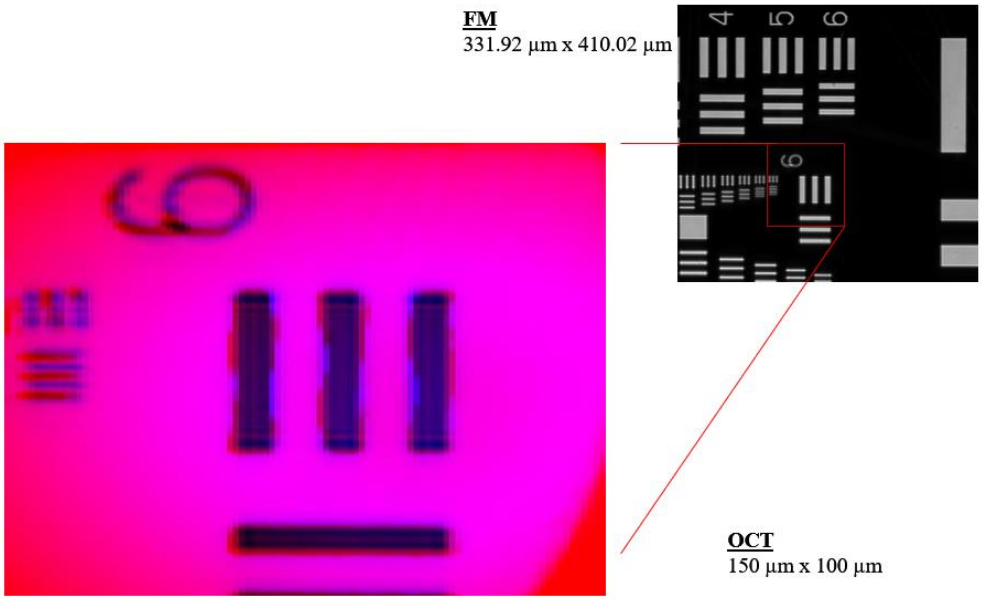

Figure 2.5 Co-registered images (150 x 100 µm) of a Group 6, Element 1 of a USAF-1951 resolution target acquired from the fluorescence (blue) and OCT (red) imaging systems. The top image is the full fluorescence microscopy image for comparison.

2.4.Conclusion

This chapters describes the design and development of an OCT from the optical components to the complete system. The process of determining a physical resolution value will require the collection of mirror data, USAF-1951 air force target, or phantom data. TEach system was designed and characterizated to determine the resolution and sensitivity. For purposes of neural imaging, the system must hace resolution in the micrometer range for structural detection of neurons. As described in this chapter, all OCT systems reached these requirements for neural imaging.

Chapter 3: Non-contact Detection of Neural Activity During Fictive Ecdysis Behavior using Phase-resolved Spectral Domain Optical Coherence Tomography

3.1. Introduction

In the previous chapter, we described each of 3 different OCT systems. In this chapter, the SD-OCT system with a central wavelength of 804 nm was used for detection of neural activity in combination with fluorescence microscopy. It has been noted that a range of structural and optical changes are known to accompany action potential propagation. These changes include scattering[53, 125, 126], size[127-129], birefringence[125, 130, 131], and turbidity[130]. Although these intrinsic changes are of exceedingly small magnitude[125], advances in optical imaging have become robust enough to detect such changes. Combing OCT and fluorescence microscopy allows simultaneous detection of phase changes and calcium flux.

Phase-resolved spectral domain OCT (pr-OCT) can detect structural changes associated with neural activity[6, 98, 99, 102, 132]. The physiologically relevant size of the mammalian peripheral nervous system[133-135] is around 3-10μm. It can detect and measure sub-nanometer displacements. Previous findings show that whenever there was an action potential it was associated to sub-nanometer changes[127-129]. Thus, these capabilities allow OCT to have the tools to study neural activities from axons, group, or individual neurons. Akkin *et al*. used a phase-sensitive OCT system that measured the transient neural surface displacement in crayfish walking leg nerves during propagation of nerve impulse. Their system was able to detect transient motion on the order of 0.4 to 1.0nm

in a saline bath [99]. Fang-Yen *et al.* used a similar system to measure the displacement of a lobster nerve with respect to a reference glass surface. A 5 nm swelling with a duration of 10ms from a single response was detected, indicating a compound response [6]. Akkin *et al.* later demonstrated similar results in squid giant axons [102, 132]. In my study we combined intrinsic optical and fluorescence imaging. Previous studies have demonstrated its uses [45-49]. We have developed a combination imaging system optimized for simultaneous phase-resolved OCT and fluorescence microscopy. In this study, we take advantage of the GAL4/UAS genetic binary system available in the fruit fly *Drosophila melanogaster* to drive expression of the calcium reporters GCaMP-3 or GCaMP-5 in specific ensembles of peptidergic neurons, the kinin and bursicon cells in the pre-pupal central nervous system (CNS). These cells exhibit stereotypic patterns of calcium mobilization upon activation of the G protein-coupled ETH receptor following exposure to nanomolar concentrations of ecdysis triggering hormone (ETH), leading to orchestration of the innate ecdysis behavioral sequence [50–54]. We correlated changes in OCT intensity and levels of phase fluctuation with calcium-induced fluorescence during the ETH-induced signaling cascade in the fly CNS. Optical detection of hormonally stimulated neuronal activity allows for a more natural window to how neurons interact in a neuronal network during a behavioral response.

In this study, I demonstrate that changes in optical properties of the *Drosophila* CNS during fictive ecdysis behavior can be detected using SD-OCT by measuring phase from specific neurons over time, quantifying these changes, and validating by correlating with calcium fluorophores.

3.2.Materials and methods

3.2.1.Animals

A single drosophila genotype *Pburs-GAL4; Kinin-GAL4>UASGCaMP3 or Kinin-GAL4; Pburs-GAL4>UAS-GCaMP5* was used in this study. In vitro neuronal imaging was performed on the isolated CNS of pre-pupae (buoyant stage; ~5-6hr prior to pupal ecdysis).

3.2.2.CNS preparation

The CNS were surgically extirpated and embedded in low melting point agarose in a petri dish containing physiological saline.

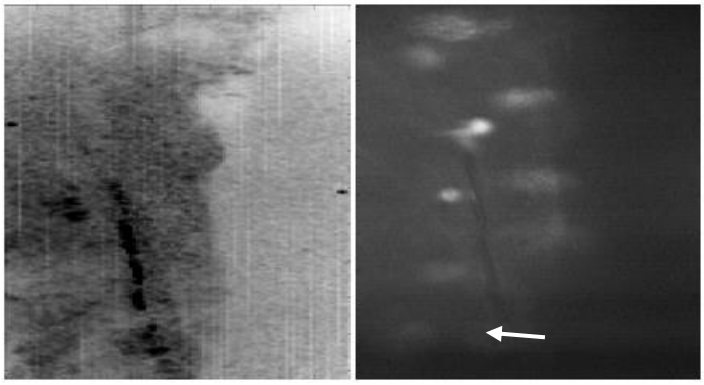

Figure 3.1 The left image shows OCT CNS while the right images shows the same region under fluorescence imaging.

3.2.3.Imaging system

The imaging system is described in Section 2.2.2.

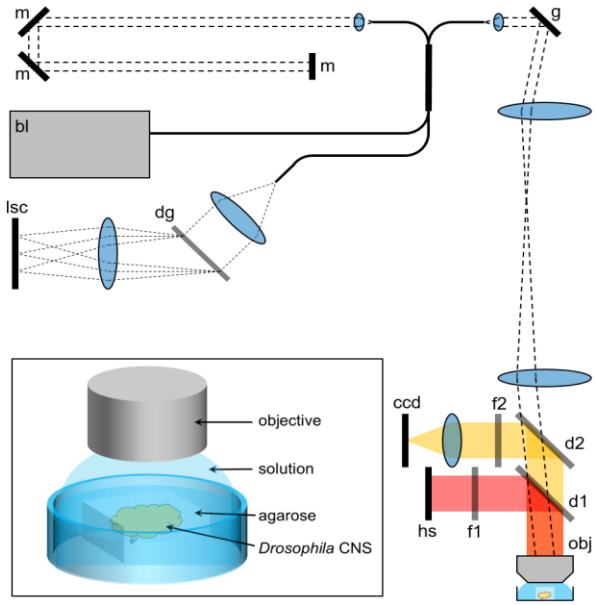

Figure 3.2 Schematic of the combined fluorescence and OCT imaging system. bl: broadband laser; g: galvo scanners; d1, d2: dichroic filters; f1, f2: wavelength filters; hs: halogen light source; obj: objective; m: mirror; dg: diffraction grating; lsc: line scan camera. Inset: a more detailed illustration of the experimental preparation for phase-resolved measurements.

3.3. Results and Discussions

Both the OCT and fluorescence data were recorded simultaneously from selected neuron (Fig 3.1 bottom right image).

3.3.1. OCT data acquisition and processing

Motion can pose a significant challenge for obtaining accurate phase-resolved measurements. While axial motion can be mitigated by comparing the phase of one depth to that of another depth, lateral movement of even 0.01 times the width of the OCT beam can induce phase noise equivalent to that induced by an average SNR of 30 dB [55]. As

this makes minimizing lateral motion between successive phase-resolved depth profiles critical, phase-resolved measurements on the *Drosophila* CNS required the additional step of carefully positioning the CNS in low-melting point agarose (see [50] for details), as depicted in the inset of Fig.3.2. In order to augment visualization of activity-induced calcium dynamics through agarose, a strain of Drosophila (Pburs-GAL4;Kinin-GAL4>UAS-GCaMP5) expressing the higher intensity fluorophore GCaMP-5 instead of GCaMP-3 was used for these experiments. Baseline data was acquired for 600s before addition of ETH to the bath. The presence of agarose necessitated a longer overall acquisition period to account for the much longer diffusion time required for the ETH to reach the CNS, at which point a cascade of activity was observed through fluorescence imaging (Fig 3.1). OCT acquisition was restricted to a single lateral location at a single bursicon neuron of interest throughout the experiment.

These experiments require positioning the OCT beam over a particular cell body highlighted by fluorescence and chosen prior to ETH introduction. While the overall position of the CNS embedded in agar remained fixed, it was observed that the individual positions of cell bodies can fluctuate over the course of experiments. However, since the OCT beam remained in a single fixed lateral location, phase-resolved data when the beam was not clearly positioned within the cell cannot be interpreted at this time. The following analysis is based on a particularly stable experiment in which the OCT beam remained clearly within the cell of interest over the entire period.

Phase analysis was restricted to a depth range spanning 23 points in depth (78.2μm) near the OCT beam focus. To mitigate the effect of axial motion caused by variations in the relative path length between the reference and sample arms, phase differences $\Delta\varphi(z, t)$ between depths 2 points from each other were calculated according to

Let the time of the start of exposure for the j^{th} fluorescence images be denoted by t_j. The standard deviation of the resulting phase differences at all 23 points in depth from j

$$\varphi(z) = tan^{-1}(\frac{Im[i_D(z)]}{re[i_D(z)]}) \tag{3.1}$$

t to t_{j+1} were computed. Scatterplots of these standard deviations versus the mean SNR over corresponding periods both before ETH presentation and during fluorescence activity are shown in Fig. 3.2. Prior to ETH presentation, phase differences are only slightly above those expected for little to no relative motions between depths. During a period of neural activity, we observed an elevation in the standard deviation of the phase differences that can be observed above 18-20dB. Phase differences for all points with a composite SNR below this threshold were consequently excluded from analysis.

Phase fluctuations were identified by the following process. Phase trends on a time scale slower than 2.5ms were removed by subtracting a moving average,

$$\Delta\phi'(z, t_i) = \Delta\phi(z, t_i) - \frac{1}{N}\sum_{j=-\frac{N}{2}}^{N/2} \Delta\phi\left(z, t_{i-j}\right) \tag{3.2}$$

where N corresponds to number of points acquired within 2.5ms. A phase fluctuation was identified either when $\Delta\phi'(z, t)$ exceeded 1.5 φ σ Δ as defined by Eq. (1.9) for more than one point in a row or if $\Delta\phi'(z, t)$ varied by more than 3 radians within 3 consecutive points. The overlay in Fig. 3.3 displays the standard deviation of the phase differences after removal of the identified fluctuations. It should be noted that these points hew closer to the theoretical phase noise floor, as would be expected.

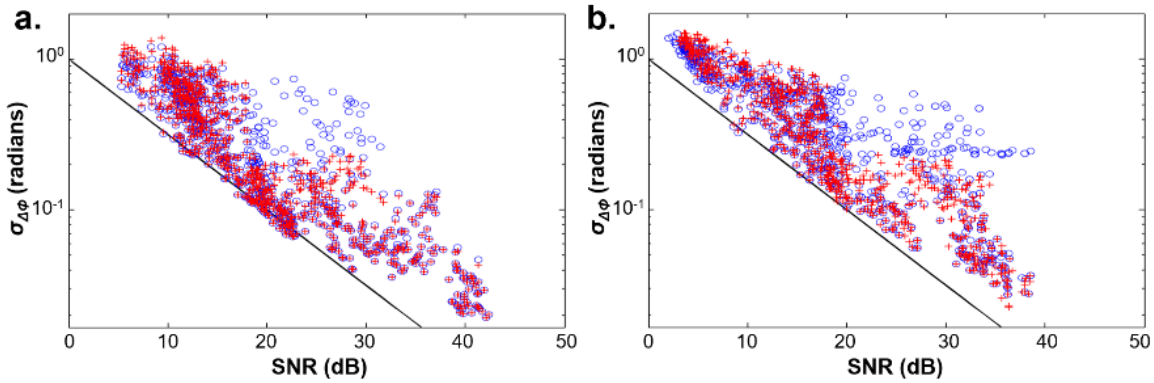

Figure 3.3 Scatterplots of the standard deviation of phase differences acquired from Drosophila CNS versus composite SNR before ETH presentation (left) and during the period of neural activity (right) are shown with blue circles. The standard deviations after removal of phase fluctuations are indicated with red crosses.

3.3.2. Fluorescence data acquisition and processing

Light from the excitation light source (Lambda XL, Sutter Instrument) is guided to a stimulation shutter through a liquid light guide. Upon passing through the shutter, incident light passes through an excitation filter (f1) and is combined with OCT light in the microscope via a dichroic mirror (d1, T510lpxrxt, Chroma) and finally is focused on the fly CNS by the objective. Fluorescence emission from the sample is separated from OCT light by another dichroic mirror (d2, 710dcxxr, Chroma), passed through the emission filter (f2), and detected by the CCD camera. The fluorescence system uses a high gain electron

multiplier- CCD camera (Hamamatsu C9100-02) for imaging. The signal detected by the fluorescence CCD camera is sent to the computer through a frame grabber (Active Silicon). Filters were chosen for imaging GFP/GCaMP-labeled samples (excitation filter: 488/35 nm, emission filter: 535/50 nm, Chroma Inc). Lateral resolution for the fluorescence system was found to be 1.86μm with a 20X water immersion objective (N.A. = 0.5). The details are discussed in section 2.2.2.

A multithreaded software program written in Microsoft Visual C++ is used to synchronize all devices during acquisition. All devices are temporally synchronized through a multifunction data acquisition card (NI-6259), which outputs analog waveforms to control the scanning galvos, line triggering of the OCT line scan camera, and a control signal for both the fluorescence CCD camera and stimulation shutter. Fluorescence data collected was matched to OCT images from information gathered off a USAF-1951 target. Intensity of the images were then averaged and plotted against OCT data.

3.3.3. Correlation between optical changes and calcium flux

The relationship between fluorescence and the remaining phase-resolved OCT data can be seen in Fig. 3.4. The position of the OCT beam was fixed on the neuron of interest indicated by the red box in the fluorescence images. Phase difference traces after thresholding correspond to OCT data acquired during acquisition of the fluorescence image. As can be seen in the representative images, little to no phase fluctuation occurs prior to ETH application, but a significant amount of phase fluctuation is evident during a period of neural activity, indicated by increased fluorescence. These phase fluctuations were identified by the following process. Phase trends on a time scale slower than 2.5 ms were removed by subtracting a moving average. Phase fluctuations were calculated using equation 3.2.

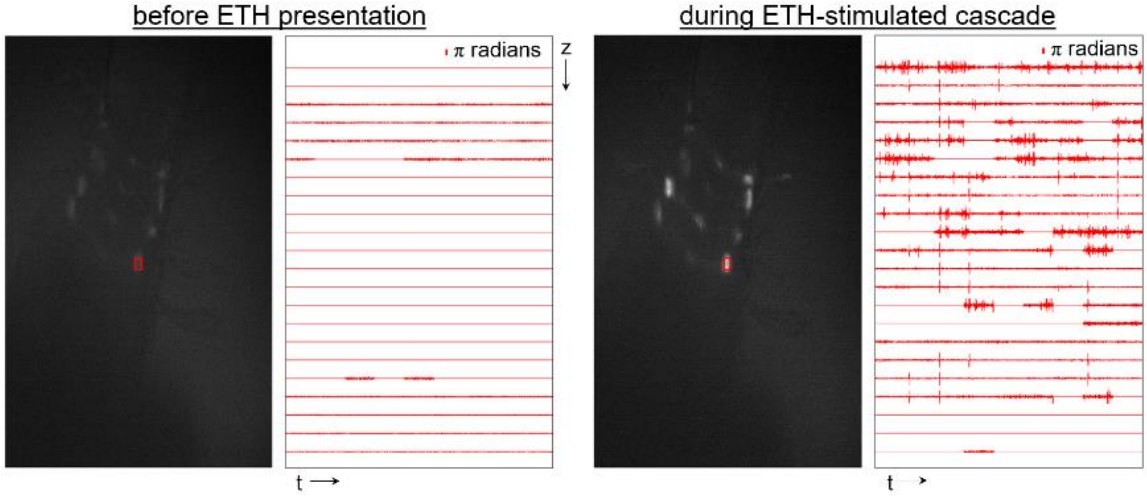

Figure 3.4 Fluorescence images (left) and depth-resolved phase difference traces (right, 1 s duration) prior to ETH application and during neural activity. Phase-resolved OCT data was acquired from the neuron indicated with the red circle. (right) are shown with blue circles. The standard deviations after removal of phase fluctuations are indicated with red crosses.

Two different calculations were made to quantify the overall level of phase fluctuations observed in Fig. 3.5. The first was to take the sum of the square of the phase differences (after the intensity threshold) over all depths, $\sum_{z,t_j \to t_{j+1}} (\Delta\phi')^2$, while the second was to count the number of phase fluctuations f N . The temporal relationship between these two measures and fluorescence can be seen in Fig. 7, where a clear difference can be noted between the baseline period (0-2500s) and near the time of neuronal calcium dynamics (2700-3400s).

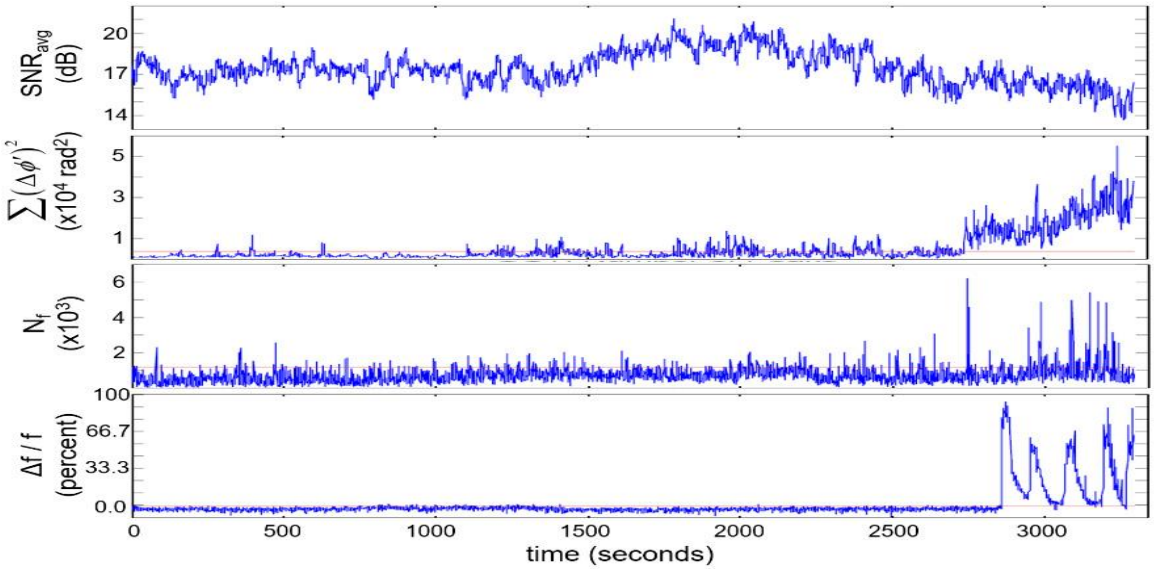

Figure 3.5 Time-resolved plots of the average SNR, summation of the squared phase fluctuations, the number of phase fluctuations, and fluorescence intensity from a neuron. ETH was applied at 600 s.

A few features are worth noting regarding data shown in Fig. 3.5, primarily the significant relative delay (~150 sec) between onset of phase fluctuation-based measures and GCaMP5- based fluorescence. Phase changes were in the order of hundreds of nanometers. We hypothesize the large phase change and the temporal delay to be caused by a combination of two factors. First, while calcium mobilization is associated with electrical activity, there is not a one-to-one correspondence between the two; nevertheless,

this cannot account for a delay of over 2 min. The more important factor is likely to be lateral motion of cell bodies in the fluorescence images caused by activity of adjacent neurons. While embedding the CNS in agar removed overall movement of the CNS, we observed lateral movement of fluorescently-labeled cellular features coincident with activity. As even slight amounts of lateral motion can lead to significant changes in phase-resolved OCT, we hypothesize that activity-induced lateral motion of the cell being monitored, potentially by neighboring cells, is a contributor to differences in onset time between phase fluctuation and fluorescence but posit that these changes are still an effect of neural activity. Chapters 5 will discuss the decoupling contributions to the phase signal of activity-induced lateral motion from activity at the location of interest through phase-resolved detection at a multiplicity of points with a line-field approach.

3.4. Conclusion

We developed an optical imaging system capable of simultaneous phase-resolved OCT and fluorescence imaging. This system was used to examine a well-characterized pattern of neural activation in the excised *Drosophila* CNS. OCT-based measures of intensity and levels of phase fluctuation differ during periods before and during this neural cascade as determined by GCaMP-5 fluorescence measurements of calcium mobilization. As responses of excised but otherwise intact CNS preparations were used, these optical signatures are not coupled to a secondary vascular response. While a one-to-one correspondence between OCT-based and fluorescence signals was not observed, label-free optical measures derived from OCT related to neural activity are evident and are the first demonstration of phase-resolved measurements to directly detect activity in a complex neural structure. Future work will include correlation against electrical detection, use of voltage-dependent indicators, and OCT-based detection at a multiplicity of points to better define OCT signals in relation to fluorescence and electrical activities during a physiologically-evoked neural cascade. The next step is to determine the phase signal of activity-induced lateral motion from activity at the location of interest through phase-resolved detection at a multiplicity of points using a line-field approach, discussed in chapter 5.

Chapter 4: Non-contact Detection of Neural Activities in Functionally Stimulated Cockroach Nervous Systems using Phase-resolved Spectral Domain Optical Coherence Tomography

4.1.Introduction

This chapter will describe the use of phase-resolved spectral domain OCT (pr-SDOCT), centered at 1310nm, to detect neural activity while the cockroach nervous system is being stimulated electrically. As discussed in the previous chapters, pr-SDOCT can be used to measures thickness changes of neurons at the sub-nanometer level. However, in this chapter, pr-SDOCT data is compared to electrophysiological recordings of nerve cord activity. In addition, this project does not image a complex brain. Because a complex brain has multiple neurons firing at different rates, these active neurons swell, displacing the neurons surrounding them that may not have been active, thus modifying the optical data. A nerve cord consists of multiple nerve fiber bundles which fire together. The sd-OCT system will image a fix position over the bundle of axons. It is currently unknown what optical characterizations are associated to neuronal activity. To yield the highest chance of optical detection, a high voltage stimulation is applied to the cockroach nerve cord so that action potentials can be recorded both electrically and optically. The nerve cord is then exposed to the sodium channel blocker, indoxacarb to validate neuronal activity. Cross-sectional images were taken before stimulation, before introduction of indoxacarb, and after the indoxacarb recording to monitor lateral and axial motion through the recording.

4.2.Materials and methods

4.2.1.Animals

Large adult male cockroaches (*Periplaneta Americana*) were selected for dissection from a colony in the Dept. of Entomology, University of California, Riverside.

4.2.2.Dissection of cockroach

The cockroach is cold-anesthetized by keeping it in an ice bucket for 30 minutes and then decapitated. The body of the cockroach is then opened up on the posterior or dorsal back and is then placed into a chamber with saline solution. The pH of the solution was maintained 7.4. Once in the chamber, the opening is widened by holding the cuticle ends with insect pins as shown in Fig.41. The digestive system and the reproductive system are removed. Starting from the terminal ganglia of the nerve cord it is carefully excited up until the thoracic ganglia where it is cut and placed into the electrophysiology chamber.

Figure 4.1 Cockroach nerve cord. a) Cockroach nerve cord over electrodes. The left two electrodes are the stimulation. The right two are the recording electrodes and the middles electrode is the ground. b) The dissection of the cockroach showing the nerve cord.

4.2.3.System description

The electrophysiology setup has 5 electrodes, two for recording, two for stimulation, and one for the ground. The cockroach nerve cord was placed over each electrode so that they are in direct to the axons. The electrodes measure the action potentials from the nerve cord at a high sensitivity and temporal resolution.

The 1310nm SD-OCT system used is shown in Fig 4.2. The system utilizes a broadband, low-coherence light source that consists of two superluminescent diodes(SLD), one centered at 1295 nm with a FWHM bandwidth of 97 nm (Thorlab Inc), and the other centered at 1350 nm with a FWHM bandwidth of 48 nm (Denselight Semiconductor Pte Ltd) resulting a combined bandwidth of 120 nm centered at 1298 nm. The system resolution was 8μm and 20μm axially and laterally, respectively. The source was connected to a circulator, which was then connected to a 2x2 fiber-based beam splitter that split 90% of the light to the sample arm and 10% of the light to the reference arm. In the sample arm,

a galvanometer (Thorlab Inc) mirrors provided transverse scanning of the collimated beam.

A lens (AC254-050-C, Thorlab) with the diameter of 1 inch and focal length of 50 mm was used to direct and collect backscatter light from the sample. The backscattered light from reference and sample arm were collected by a custom-built spectrometer. The spectrometer consists of a diffraction grating (Wasatch Photonics, 1100 lpmm), a focusing lens (JenOptik Optical Systems, f=150 mm), polarization beam splitter cube (Rocky Mountain Instrument Co., 4-inch Cube) and two 1024 pixels line scan cameras (Goodrich SUI SU-LDH linear digital high-speed InGaAs camera).

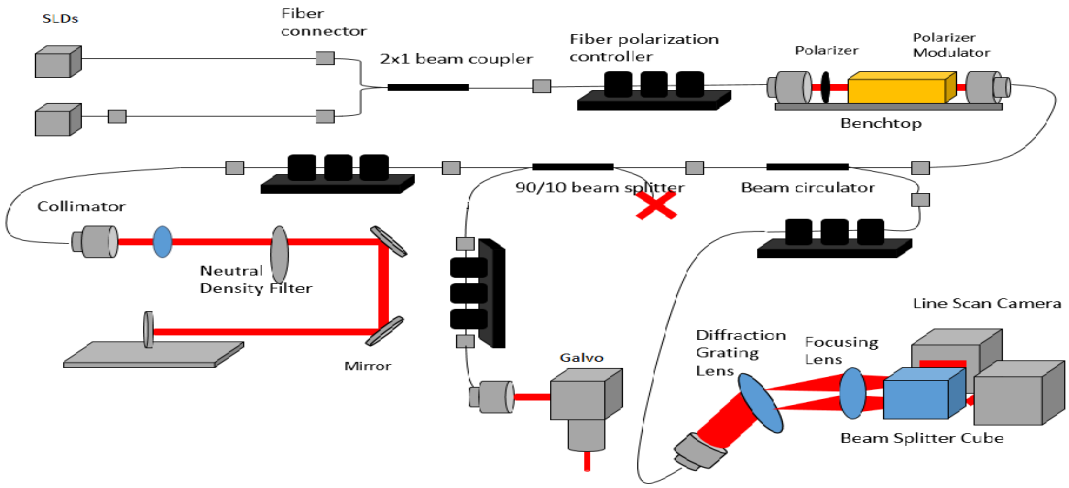

Figure 4.2 Schematic of the 1310 spectral-domain OCT system showing all the optical components within the modality.

4.2.4.OCT data acquisition and processing

The laser is positioned over the cockroach nerve cord and recorded over time. Each recording is an hour long. The electrophysiology chamber is sealed with a cover slide so as to maintain stable humidity, thus ensuring that the nerve cord does not desiccate during the experiment. Each OCT image is collected as an M-scan. OCT M-scan images were

acquired at 7kHz from the cockroach nerve cord. The duration of an action potential is 2~3ms. Therefore, at the acquisition speed of 7kHz, an action potential from a bundle of axons at a single observational point is enough to represent the thickness change during an action potential event. Because the exposure time is inversely related to the acquisition speed, if the acquisition speed was increased, then the camera exposure time would decrease. A smaller exposure time would mean that less photons are collected from the sample; which, would translate to a lower SNR[8].

As described in chapter 2, the wavenumber spacing from the collected spectrum is linearly interpolated to evenly space each wavenumber from the nonlinear k-space sampled spectral data collected at the spectrometer. A fast Fourier-transformation(FFT) is then preformed on the wavenumber of the spatial domain, yielding depth-resolved structural and phase information.

4.2.5.Electrophysiology data acquisition and processing

The nerve cord was placed on top of 5 electrodes as seen in fig.4.1. To induce neural activity, a stimulator from A.M.P.I. Master-9 is used to send a constant voltage through the stimulating electrodes. At the other end of the chamber two electrodes are used as recorder and sends a signal to the A-M systems differential AC amplifier Model 1700. The AC amplifier include a low pass and high pass filter set at 100Hz and 5kHz with the gain set at x1000. The amplifier also includes a group that is connected to the chamber to reduce noise.

The electrical signal is both observed from an oscilloscope and the acquisition computer but is only recorded through the computer. The stimulator is temporally synchronized with the OCT trigger so that both the optical and electrical data can be temporally matched. The electrical data is processed in MATLAB for averaging to further reduce the noise. Figure 4.3 shows the electrical recording by the electrode.

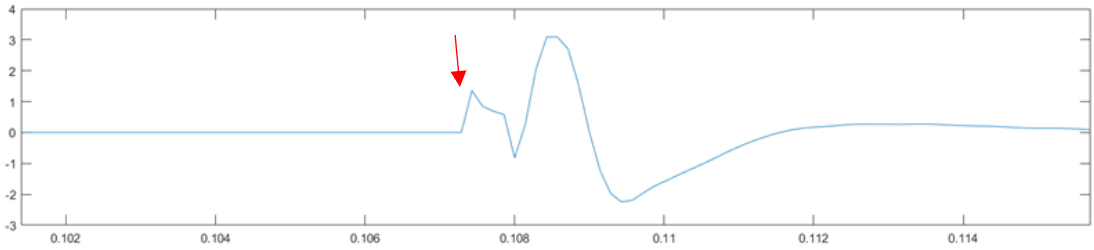

Figure 4.3 Electrical recording from a stimulated cockroach nerve cord. The y-axis is in voltage and the x-axis is in seconds. The first peck (red arrow) is the stimulation artifact, the second is the action potential.

4.3.Results and discussion

4.3.1.Phase noise measurement of pr-SDOCT

A coverslip is used to check the phase noise of the system. M-scan data (where the laser is stationary at one fixed location) is collected from the coverslip at the focal plane and the amount of light is attenuated by using a neutral density filter in the sample arm so that different signal to noise ratio(SNR) are acquired. The data was analyzed to extract intensity and phase information as described in chapter 1 and 3.

The cockroach nerve surface was measured over time in between experiments. The cockroach surface between different points in time was measured by taking the ifft of the image's fft. This value is then multiplied by the conjugate of the second image's fft for comparison. There was no lateral or axial movement during the experiment

4.3.2.Cockroach phase processing and noise removal

Similar to the *drosophila* data, two points in depth were used to calculate the phase difference; however, the two points used for the cockroach is the surface of the nerve and the wrapped image of the glass slide. The equation used to calculate the phase difference is described in great length in chapter 1 and 3. Note that in chapter 3 the phase difference was calculated two points away from the surface. When this formula is used on the cockroach data no significate phase difference was detected. In this chapter the points used to determine the phase difference is larger, this is because the cockroach nerve is several micrometers larger then that *Drosophila* neurons, thus the glass slide is used as the reference. This reference position is subtracted with all the different layers of the cockroach nerve. Notices that it would be possible to subtract within the nerve; however, the two points must be larger than the nerve change.

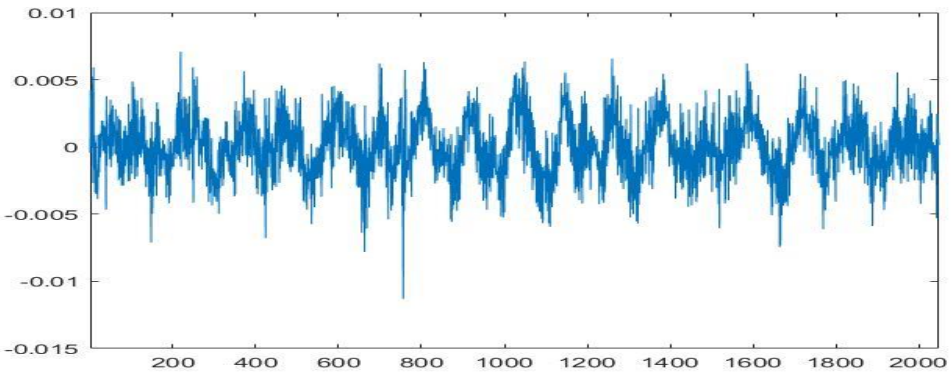

Figure 4.4 Phase recording from a stimulated cockroach nerve cord. The y-axis is in radian and the x-axis is A-line number. A 60Hz frequency can be seen from this plot.

To reduce the noise further, the phase was weighted using the intensity or SNR. This process is identical to Chapter 3. However, the phase information is collected from

the 1310 SD-OCT system. This system had an underlaying 60Hz noise that is clearly seen throughout the phase information. Fig. 4.4 shows the noise over the phase information. The source of the noise is not entirely clear. One potential source is the glavo-scanner. Regardless it is possible to remove the noise computationally.

The first step of removing the 60Hz noise is to isolate the overlaying frequency. Once the frequency is determined and isolated it subtracted from the raw phase data. By applying a fast Fourier transformation on the phase information, it is possible to separate each frequency and to selectively remove the 60Hz noise from the phase information. Thus, by stringing all the phase information into a continuous line it is possible to have a large sample size and clearly isolate the 60Hz noise. Once the noise is selected the remaining information is removed and the noise information is inversely fast Fourier transformed to

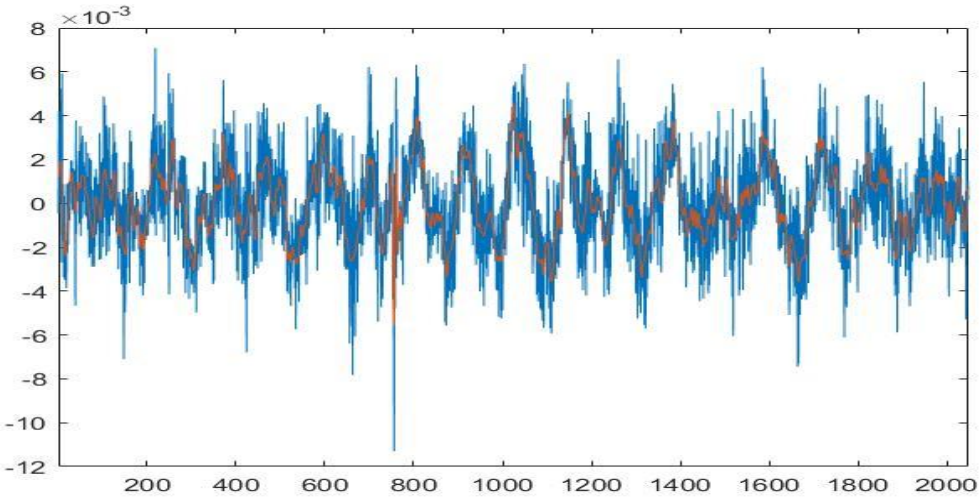

Figure 4.5 Phase recording from a stimulated cockroach nerve cord. The y-axis is in radian and the x-axis is A-line number. A 60Hz frequency can be seen from this plot in blue. In red only the 60Hz frequency can be seen.

return to the phase data. The noise phase data is then overlapped with the original phase data as shown in fig.4.5.

With the 60Hz noise identified, the noise is subtracted out of the original data by subtracting the noise to the raw phase difference data. What remains is the standard noise and the optical information that holds the action potential as shown in fig.4.6.

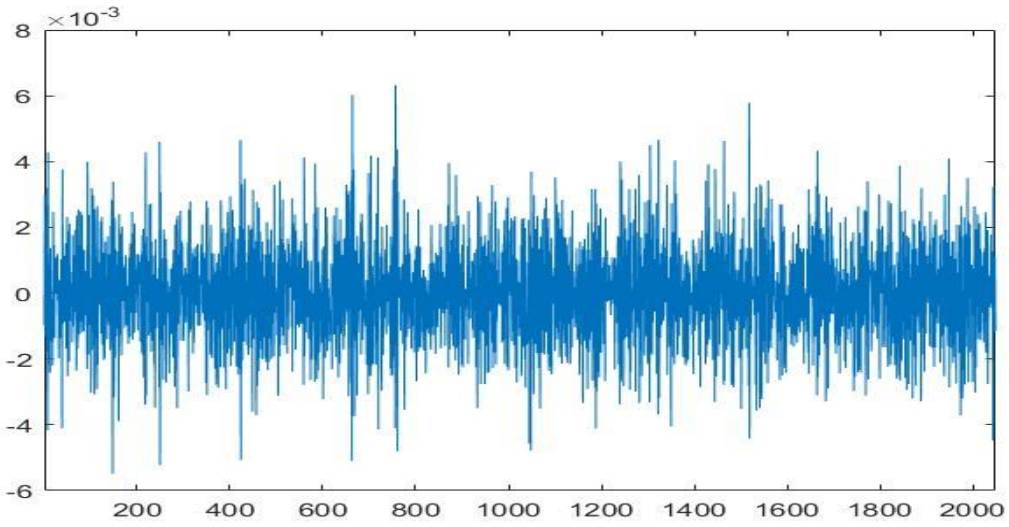

Figure 4.6 Phase recording from a stimulated cockroach nerve cord. The y-axis is in radian and the x-axis is A-line number. Phase information without the 60Hz noise.

4.3.3. Comparing Optical to electrical data

Because both the optical and electrical information shared the same trigger it is possible to align both systems together using this trigger. When the trigger fired it told both systems to record a single frame of information. It should also be noted that both the optical and electrical information is recording continually. During a single frame there is one

electrical stimulation sent to the cockroach nerve cord. The parameters such as voltage and duration of the stimulation can be adjusted by the A.M.P.I. Master-9 stimulator.

Because the system is running at 7kHz per M-line it is possible to calculate the duration of a single frame of information from both the electrical and the optical data. To calculate the time, it takes to capture a single M-line divide the rate of the camera over 1. To calculate the amount of time it takes to capture a frame, multiple the number of M-lines by the rate at which it captures a single M-line image. In this experiment it takes 293 milliseconds to capture a single frame.

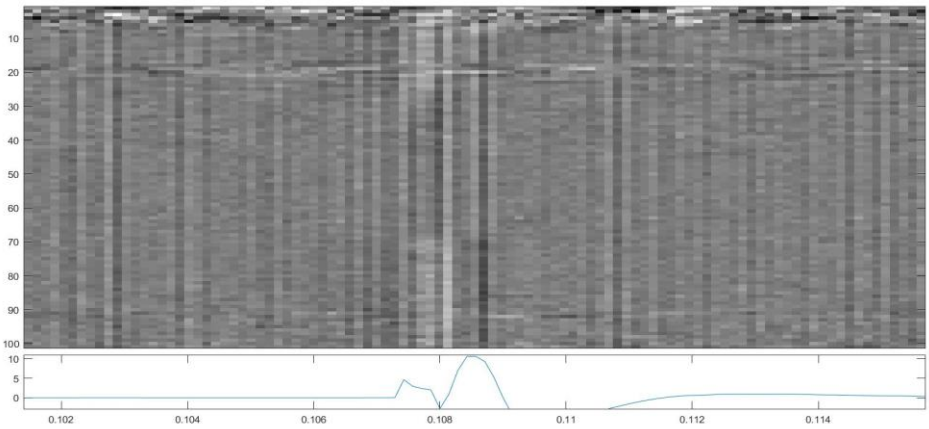

Figure 4.7 Phase recording from a stimulated cockroach nerve cord showing both electrical and phase information. The color bar is in radian. The phase image seen above has the y-axis in depth by pixel. The bottom plot shows the electrical data with the y-axis showing voltage. Both figures share the same x-axis. The x-axis is in seconds.

To verify that the OCT system can detect an optical change in correlation to the electrical stimulation, a high voltage was sent through the nerve cord. A plot of both the optical and electrical data is taken together on the same time scale, shown in Fig.4.7. The optical traces are a few milliseconds ahead of the electrical data. This finding is similar to other publications and findings from our lab and other optical coherence labs. The lower

plot shows a cockroach nerve stimulated under high voltages. The upper plot shows the optical data in depth over time. Examining the optical data, it is clear that there is a change within the upper and lower areas of the optical depth. This phase change would associate a mechanical displacement. The displacement is around 1micrometer.

4.3.4.Analyzing Optical signal

Phase data was processed in multiple steps to remove the noise. The first process was to remove overall noise using an imfilter. The next process corrects for axial motion which is the phase difference between two points within the phase depth profile. To determining which two points to calculate, the phase difference was calculated similarly to chapter 3. The current phase layer was subtracted with the third layer below the current phase layer. However, no significant phase difference was observed using this method. However, when using two layers with a larger separation, a significant change was

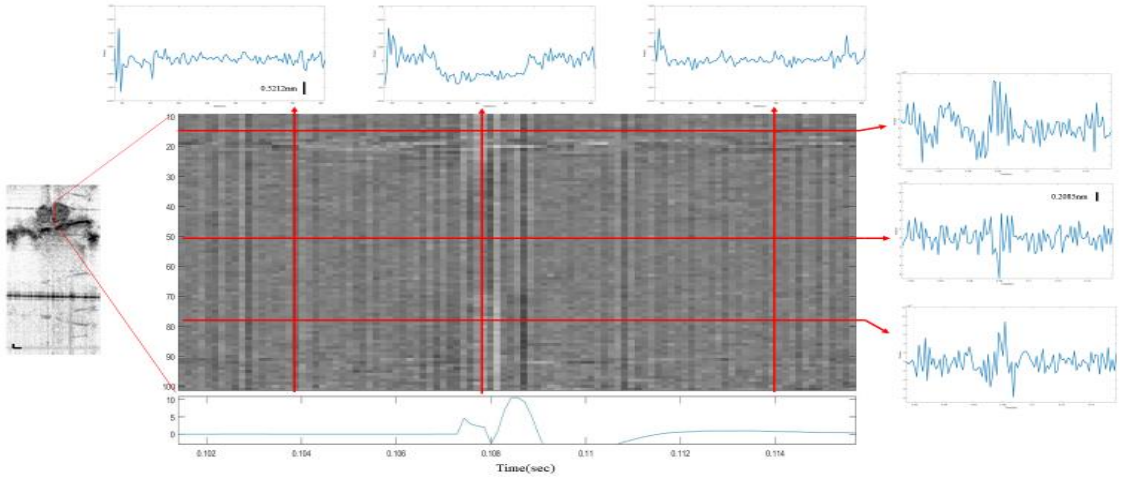

Figure 4.8 Phase imaging over time. Each red arrow points to that phase plot. The cross-sectional image of the cockroach nerve on the side of the diagram is an example of a M-scan off the nerve.

observed. The two points used was the glass-slide of the chamber and the cockroach nerve layers. Fig.4.8 shows a cockroach nerve stimulated at high voltage.

Several different plots are shown in Fig.4.8 taken from the horizontal vertical positions. The vertical position gives the phase depth where the axis are depth vs radians. The scale bar shows how 0.005 radians is equal to 0.5 nanometers. To calculate the phase difference multiple the radian by the central wavelength. This value is then divided by 4π to calculate the physical phase difference in nanometers. During the stimulation there is a clear decrease in the phase difference in depth. The size of the phase difference is 300nm which is reasonable for a bundle of axons which are around 50 micrometers in size. Note that the slope between the transition between the phase difference is 50 micrometers, which, is the same of a cockroach axon. The actual phase difference in the cockroach nerve cord is around 1 nanometer. The phase depth after the stimulation returns to the same state as the plot before the stimulation. Plot taken laterally over time yields temporal information on the duration of the neuronal activity. Each optical phase change is associated to several milliseconds similar to an action potential duration.

4.3.5.Indoxacarb with high voltage stimulation

Fig.4.9 shows a cockroach nerve that was stimulated using a high voltage stimulation. The red line depicts the depth at a specific time point from the OCT image and plots the phase change in radians on the top right side of the figure. The blue line depicts the depth plot during the stimulation and is shown in the middle right side of the figure. Note that there is a phase increase in the center of the plot. The phase change is 300

micrometers. The purple line depicts the depth plot after the stimulation. The plots before and after the stimulation are both flat lines.

Fig.10 shows the same cockroach nerve position during high voltage stimulation; however, indoxacarb was added to the nerve. The red line depicts the depth location in time

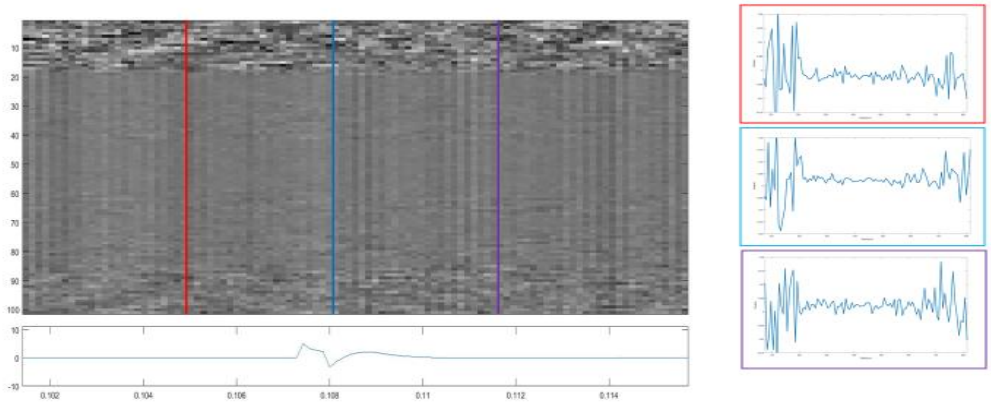

Figure 4.10 High voltage stimulation with indoxacarb phase imaging over time (top lift) with corresponding electrical trace (bottom lift). The colored line and colored boxes (right side) are color matched. Each line represents the time point in which the plots on the right side were taken from. The right plots are radians over depth.

before the stimulation. The blue line depicts the depth location in time during the high voltage stimulation. The purple line depicts the depth location in time after the stimulation of the cockroach nerve cord. The plots before and after the stimulation does not have any changes. During the stimulation, there was no electrical or optical changes found. The blue plot is identical to the plots before and after the stimulation.

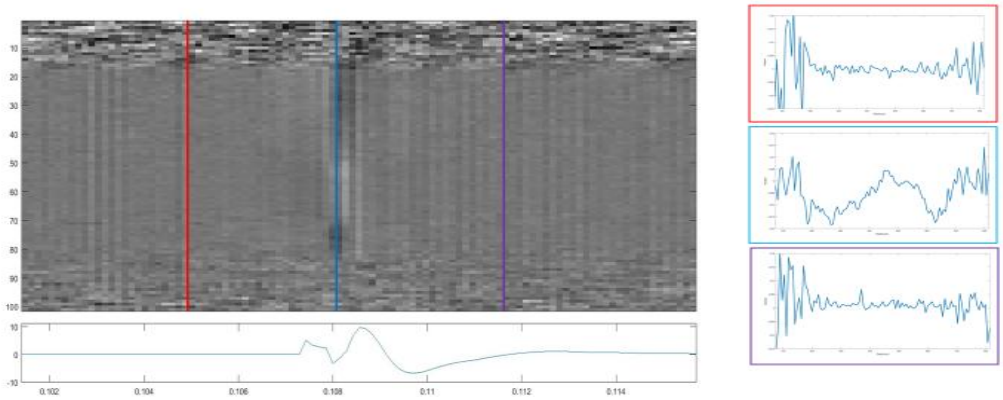

Figure 4.9 High voltage stimulation phase imaging over time (top lift) with corresponding electrical trace (bottom lift). The colored line and colored boxes (right side) are color matched. Each line represents the time point in which the plots on the right side were taken from. The right plots are radians over depth.

4.4.Conclusion

In this study, phase-resolved optical coherence tomography has been demonstrated to be capable of detection of neural activity at different stimulated voltages. Phase-resolved OCT was able to measure 1nm phase changes associated to electrical stimulation. Current and future improvement efforts are focus towards the improvement of detection sensitivity of this pr-OCT and detection of activity along nerves and the development of the line field pr-OCT system described in the next chapter.

Chapter 5: Line-field swept-source optical coherence tomography design and development

5.1.Introduction

In the last chapter, we describe the design of the line-field swept-source OCT system and its characterization using a mirror. This chapter will focus on using a line field swept source system (LF-SSOCT).

5.2.Materials and methods

5.2.1. System description

Figure 2.3 shows the schematic diagram of the swept source OCT system (SS-OCT). The SS-OCT system uses a swept wavelength semiconductor laser, broad sweepers 840-HP from Superlum. The maximum power of the source is 20mW and wavelength range of 800-878nm. The source is connected through an optical fiber to a collimator that introduces a collimated beam to a non-polarizing beam splitter cube, with a coating designed for 700 - 1100 nm. 70 percent of the light is split to the reference arm while 30 percent of the light is sent to the sample arm. The light within the sample arm passes through a 1D large beam, 10 mm diameter, galvo system using a silver-coated mirror. The bean then travels through a tube lens and a line iris until it reaches a 50mm focus cylindrical achromat lens with a 650 - 1050 nm coating. While the light from the reference arm is split again with a non-polarizing beam splitter cube where it splits 90 percent of the light to a mirror and is reflected backwards so that it is recombed with the sample arm light. The combined light is detected by a Basler spL2048-140km camera link camera delivers 140

kHz at 2k resolution. The camera is controlled using a frame grader from National Instruments, model number NI1429. The galvo is controlled and triggered by a BNC breakout boxes (BNC 2090A).

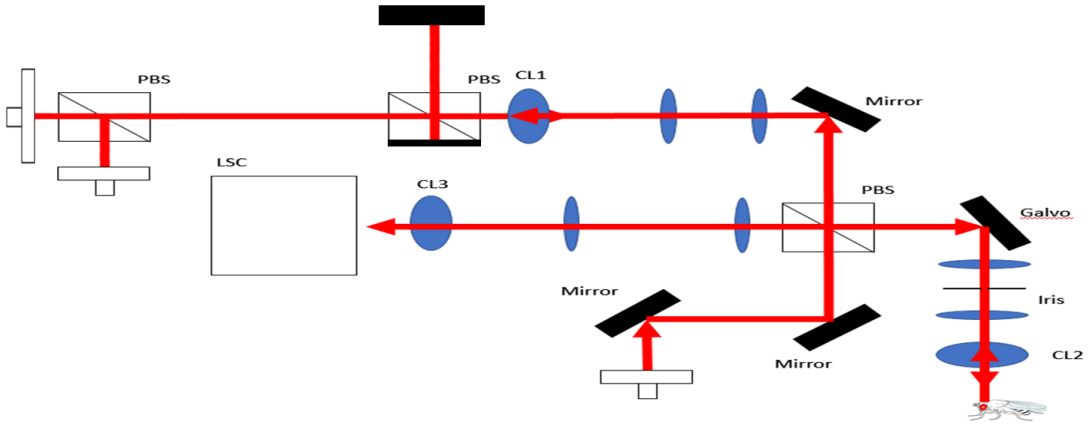

Figure 5.1 Schematic of swept source line field system and the Mach-Zehnder interferometer.

The other 10 percent of the light passes through the cube and enters Mach-Zehnder interferometer system as shown in figure 2.3. The light combines after traveling through the Mach-Zehnder interferometer and is detected by a fiber-coupled balanced amplifier photodetector with a bandwidth of 400MHz. This detector sends optical data to a PCI Express A/D Board AD14-400 from Ultraview. A critical element of the system includes the iris. This iris prevents noise from lateral positions.

5.2.2.OCT data recording and processing

OCT data was acquired at a swept rate of 70kH, triggered off a function generated. The spL2048-140km camera link camera captures the focus light, where the National

Instrumentations Measurement & Automation Explorer (NI-MAX) is able to save an image of the spectrum. Each spectrum is saved as a PNG image and processed in MATLAB. The image is converted to a double and the average is calculated. The spectrum length is estimated, and the image is converted to a depth profile by applying a fast Fourier transform.

5.3.Results and Discussion

5.3.1.Characterization of Line field system

To measure the signal to noise ratio (SNR) a mirror was used as the reflective surface with a neutral density filter as seen in Fig.5.2. The plot on Fig.5.2a shows the average calculated depth profile of the spectrum, while Fig.5.2b is of the correctional image of the same profile. This data does not include the Mach-Zehnder information, so a theoretical calibration was used for this data set. the Off a mirror the peak value is 123 dB while the noise floor is around 85, thus the resulting SNR is 38 plus the amount of light that was blocked by the neutral density filter. Note that one M-scan image from a line field system yields a cross-sectional image while in a point scanning system would require a galvo to move the beam to form the same image.

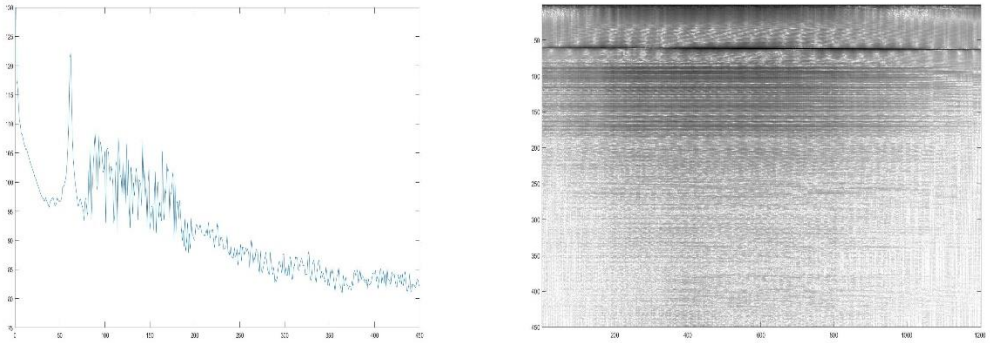

Figure 5.2 a) depth profile off a mirror using the line field swept source system. b) cross-sectional image of a mirror using the line field swept source system.

5.4.Conclusion.

In this chapter a swept source laser was combined with a line field system. This configuration was built for the first time to my acknowledgment. This system allows cross-sectional imaging without moving the beam, thus providing lateral information when imaging phase at the nanometer level. Future work on this system would providing real-time imaging of multiple neuronal activity of individual action potential.

Conclusion

The detection of neural activity using optical coherence tomography is a suitable method and is independent of the use of exogenous agents. Although the intrinsic structural changes of a nerve during an action potential is extremely small, with high SNR it is possible to resolve sure intrinsic changes to detect nanometer changes. Phase resolved spectral domain OCT can detect these nanometer changes off the thickness of the axon during the propagation of an action potential while it is stimulated or a single neuron that is behaviorally stimulated. It is also possible to resolve the action potential temporally via continues phase-resolved measurements. All of this would not be possible if it was not for the rigorous alignment and characterization of each OCT system described in this dissertation.

The first set of data shown was the detection of the *Drosophila* bursicon neuron when stimulated by the ecdysis triggering hormone. Phase resolved spectral domain OCT was able to detect the large swelling when ecdysis trigging hormone was presented to the nervous system of the *Drosophila*. The neuron swelled during presentation of the hormone and was confirmed by using a calcium fluorescent indicator as a one-to-one comparison. Furthermore, a cockroach nerve was excised and stimulated using a stimulator while optical recorded using phase resolved spectral domain OCT was shown to also detect the swelling during neuron activity from cockroach nerve bundles along their nerve system. In both experiments it was shown that the phase change increased. Because lateral scanning

introduces phase noise, the OCT phase information was limited to a specific location and made these types of experiments vulnerable to lateral motion.

Because of these concern the last chapter addresses lateral motion by building a line field swept source system. This system is capable of imaging a cross-sectional image without lateral scanning, thus avoiding lateral motion noise. Without lateral phase noise the limiting factor is the signal to noise ratio. With more alignment the system would be capable to detect the nanometer thickness changes associated to neuron activity. However, at the moment the system is aligned for intensity imaging for structural imaging. In conclusion optical coherence tomography is a suitable method to detect neuronal activity.

References and Bibliography

1. Huang, D., et al., *Optical coherence tomography.* Science, 1991. **254**(5035): p. 1178-81.

2. Schmitt, J.M., et al., *Optical-coherence tomography of a dense tissue: statistics of attenuation and backscattering.* Phys Med Biol, 1994. **39**(10): p. 1705-20.

3. de Boer, J.F., R. Leitgeb, and M. Wojtkowski, *Twenty-five years of optical coherence tomography: the paradigm shift in sensitivity and speed provided by Fourier domain OCT [Invited]*. Biomed Opt Express, 2017. **8**(7): p. 3248-3280.

4. Clivaz, X., et al., *High-resolution reflectometry in biological tissues.* Opt Lett, 1992. **17**(1): p. 4-6.

5. Tanno, N., et al., *Biliary lipid composition in heterozygous familial hypercholesterolemia and influence of treatment with probucol.* Dig Dis Sci, 1994. **39**(7): p. 1586-91.

6. Fang-Yen, C., et al., *Noncontact measurement of nerve displacement during action potential with a dual-beam low-coherence interferometer.* Opt Lett, 2004. **29**(17): p. 2028-30.

7. Choma, M., et al., *Sensitivity advantage of swept source and Fourier domain optical coherence tomography.* Opt Express, 2003. **11**(18): p. 2183-9.

8. de Boer, J.F., et al., *Improved signal-to-noise ratio in spectral-domain compared with time-domain optical coherence tomography.* Opt Lett, 2003. **28**(21): p. 2067-9.

9. Leitgeb, R., C. Hitzenberger, and A. Fercher, *Performance of fourier domain vs. time domain optical coherence tomography.* Opt Express, 2003. **11**(8): p. 889-94.

10. Drexler, W. and J.G. Fujimoto, *Optical Coherence Tomography Technology and Applications Preface.* Optical Coherence Tomography: Technology and Applications, 2008: p. V-Vii.

11. Fercher, A.F., *Optical coherence tomography - development, principles, applications.* Z Med Phys, 2010. **20**(4): p. 251-76.

12. Park, B., et al., *Real-time fiber-based multi-functional spectral-domain optical coherence tomography at 1.3 microm.* Opt Express, 2005. **13**(11): p. 3931-44.

13. Yazdanfar, S., et al., *Frequency estimation precision in Doppler optical coherence tomography using the Cramer-Rao lower bound.* Opt Express, 2005. **13**(2): p. 410-6.

14. Hee, M.R., et al., *Optical coherence tomography of the human retina.* Arch Ophthalmol, 1995. **113**(3): p. 325-32.

15. Hitzenberger, C., et al., *Three-dimensional imaging of the human retina by high-speed optical coherence tomography.* Opt Express, 2003. **11**(21): p. 2753-61.

16. Nassif, N., et al., *In vivo high-resolution video-rate spectral-domain optical coherence tomography of the human retina and optic nerve.* Opt Express, 2004. **12**(3): p. 367-76.

17. Gotzinger, E., M. Pircher, and C.K. Hitzenberger, *High speed spectral domain polarization sensitive optical coherence tomography of the human retina.* Opt Express, 2005. **13**(25): p. 10217-29.

18. Aguirre, A.D., et al., *Depth-resolved imaging of functional activation in the rat cerebral cortex using optical coherence tomography.* Opt Lett, 2006. **31**(23): p. 3459-61.

19. Lim, H., et al., *High-speed imaging of human retina in vivo with swept-source optical coherence tomography.* Opt Express, 2006. **14**(26): p. 12902-8.

20. Huber, R., et al., *Fourier domain mode locking at 1050 nm for ultra-high-speed optical coherence tomography of the human retina at 236,000 axial scans per second.* Opt Lett, 2007. **32**(14): p. 2049-51.

21. Fernandez, E.J., et al., *Ultrahigh resolution optical coherence tomography and pancorrection for cellular imaging of the living human retina.* Opt Express, 2008. **16**(15): p. 11083-94.

22. Fingler, J., et al., *Volumetric microvascular imaging of human retina using optical coherence tomography with a novel motion contrast technique.* Opt Express, 2009. **17**(24): p. 22190-200.

23. Torti, C., et al., *Adaptive optics optical coherence tomography at 120,000 depth scans/s for non-invasive cellular phenotyping of the living human retina.* Opt Express, 2009. **17**(22): p. 19382-400.

24. Granstedt, A.E., et al., *Fluorescence-based monitoring of in vivo neural activity using a circuit-tracing pseudorabies virus.* PLoS One, 2009. **4**(9): p. e6923.

25. Wang, R.K. and L. An, *Multifunctional imaging of human retina and choroid with 1050-nm spectral domain optical coherence tomography at 92-kHz line scan rate.* J Biomed Opt, 2011. **16**(5): p. 050503.

26. Choi, W., et al., *Phase-sensitive swept-source optical coherence tomography imaging of the human retina with a vertical cavity surface-emitting laser light source.* Opt Lett, 2013. **38**(3): p. 338-40.

27. Santos, M., et al., *Simulation of cellular changes on Optical Coherence Tomography of human retina.* Conf Proc IEEE Eng Med Biol Soc, 2015. **2015**: p. 8147-50.

28. Sugita, M., et al., *Analysis of optimum conditions of depolarization imaging by polarization-sensitive optical coherence tomography in the human retina.* J Biomed Opt, 2015. **20**(1): p. 016011.

29. Campbell, J.P., et al., *Detailed Vascular Anatomy of the Human Retina by Projection-Resolved Optical Coherence Tomography Angiography.* Sci Rep, 2017. **7**: p. 42201.

30. Cense, B., et al., *Measuring polarization changes in the human outer retina with polarization-sensitive optical coherence tomography.* J Biophotonics, 2017.

31. Mansoori, T., et al., *Measurement of Radial Peripapillary Capillary Density in the Normal Human Retina Using Optical Coherence Tomography Angiography.* J Glaucoma, 2017. **26**(3): p. 241-246.

32. Theelen, T. and M.M. Teussink, *Inspection of the Human Retina by Optical Coherence Tomography.* Methods Mol Biol, 2018. **1715**: p. 351-358.

33. Zhan, C.A., T. Ledgeway, and C.L. Baker, Jr., *Contrast response in visual cortex: quantitative assessment with intrinsic optical signal imaging and neural firing.* Neuroimage, 2005. **26**(2): p. 330-46.

34. Wang, B., Y. Lu, and X. Yao, *In vivo optical coherence tomography of stimulus-evoked intrinsic optical signals in mouse retinas.* J Biomed Opt, 2016. **21**(9): p. 96010.

35. Boppart, S.A., *Optical coherence tomography: technology and applications for neuroimaging.* Psychophysiology, 2003. **40**(4): p. 529-41.

36. Valenti, D.A., *Neuroimaging of retinal nerve fiber layer in AD using optical coherence tomography.* Neurology, 2007. **69**(10): p. 1060.

37. Regar, E., J. Schaar, and P.W. Serruys, *Images in cardiology. Acute recoil in sirolimus eluting stent: real time, in vivo assessment with optical coherence tomography.* Heart, 2006. **92**(1): p. 123.

38. Picchi, A., A. Micheli, and U. Limbruno, *Images in cardiology. The traumatic effect of balloon dilatation on neointimal hyperplasia: what we did not see before optical coherence tomography.* Heart, 2011. **97**(3): p. 265-6.

39. Tereshchenko, A.S., et al., *[Basic principles of optical coherence tomography in interventional cardiology]*. Vestn Rentgenol Radiol, 2013(6): p. 67-72.

40. Yonetsu, T., et al., *Optical coherence tomography- 15 years in cardiology.* Circ J, 2013. **77**(8): p. 1933-40.

41. Vignali, L., E. Solinas, and E. Emanuele, *Research and clinical applications of optical coherence tomography in invasive cardiology: a review*. Curr Cardiol Rev, 2014. **10**(4): p. 369-76.

42. Baumgartner, A., et al., *Polarization-sensitive optical coherence tomography of dental structures.* Caries Res, 2000. **34**(1): p. 59-69.

43. Otis, L.L., et al., *Dental optical coherence tomography: a comparison of two in vitro systems.* Dentomaxillofac Radiol, 2000. **29**(2): p. 85-9.

44. de Melo, L.S., et al., *Evaluation of enamel dental restoration interface by optical coherence tomography.* J Biomed Opt, 2005. **10**(6): p. 064027.

45. Hsieh, Y.S., et al., *Dental optical coherence tomography.* Sensors (Basel), 2013. **13**(7): p. 8928-49.

46. Lee, S.H., et al., *Dental optical coherence tomography: new potential diagnostic system for cracked-tooth syndrome.* Surg Radiol Anat, 2016. **38**(1): p. 49-54.

47. Watanabe, H., et al., *Resolution characteristics of optical coherence tomography for dental use.* Dentomaxillofac Radiol, 2017. **46**(3): p. 20160358.

48. Welzel, J., *Optical coherence tomography in dermatology: a review.* Skin Res Technol, 2001. **7**(1): p. 1-9.

49. Alex, A., et al., *Three-dimensional multiphoton/optical coherence tomography for diagnostic applications in dermatology.* J Biophotonics, 2013. **6**(4): p. 352-62.

50. Ulrich, M., et al., *Dynamic Optical Coherence Tomography in Dermatology.* Dermatology, 2016. **232**(3): p. 298-311.

51. Schwartz, M., A. Levine, and O. Markowitz, *Optical coherence tomography in dermatology.* Cutis, 2017. **100**(3): p. 163-166.

52. Boppart, S.A., M.E. Brezinski, and J.G. Fujimoto, *Optical coherence tomography imaging in developmental biology.* Methods Mol Biol, 2000. **135**: p. 217-33.

53. Agrawal, A., et al., *Optic Nerve Head Measurements With Optical Coherence Tomography: A Phantom-Based Study Reveals Differences Among Clinical Devices.* Investigative Ophthalmology & Visual Science, 2016. **57**(9): p. Oct413-Oct420.

54. Mason, C., et al., *Doppler optical coherence tomography for measuring flow in engineered tissue.* Biosensors & Bioelectronics, 2004. **20**(3): p. 414-423.

55. Boppart, S.A., Y. Yang, and R.K. Wang, *Optical Coherence Tomography in Tissue Engineering.* Optical Coherence Tomography: Technology and Applications, 2008: p. 889-917.

56. Gurjarpadhye, A.A., et al., *Dynamic Assessment of the Endothelialization of Tissue-Engineered Blood Vessels Using an Optical Coherence Tomography Catheter-Based Fluorescence Imaging System.* Tissue Engineering Part C-Methods, 2015. **21**(7): p. 758-766.

57. Kagawa, Y., et al., *Real-time quantitation of internal metabolic activity of three-dimensional engineered tissues using an oxygen microelectrode and optical coherence tomography.* Journal of Biomedical Materials Research Part B-Applied Biomaterials, 2017. **105**(4): p. 855-864.

58. Mehta, R., et al., *Wireless, Web-Based Interactive Control of Optical Coherence Tomography with Mobile Devices.* Translational Vision Science & Technology, 2017. **6**(1).

59. Dichtl, S., et al., *Imaging of dental material by polarization sensitive optical coherence tomography.* Lasers in Dentistry V, Proceedings Of, 1999. **3593**: p. 169-176.

60. Stifter, D., et al., *Polarisation-sensitive optical coherence tomography for material characterisation and strain-field mapping.* Applied Physics a-Materials Science & Processing, 2003. **76**(6): p. 947-951.

61. Stifter, D., et al., *Investigation of polymer and polymer/fibre composite materials with optical coherence tomography.* Measurement Science and Technology, 2008. **19**(7).

62. Qin, Y.W. and H. Zhao, *Spectral-domain Optical Coherence Tomography for Material Detection.* Manufacturing Engineering and Automation Ii, Pts 1-3, 2012. **591-593**: p. 1139-1142.

63. Hutiu, G., et al., *Surface imaging of metallic material fractures using optical coherence tomography.* Applied Optics, 2014. **53**(26): p. 5912-5916.

64. Rollins, A., et al., *In vivo video rate optical coherence tomography.* Opt Express, 1998. **3**(6): p. 219-29.

65. Laubscher, M., et al., *Video-rate three-dimensional optical coherence tomography.* Opt Express, 2002. **10**(9): p. 429-35.

66. Akiba, M. and K.P. Chan, *In vivo video-rate cellular-level full-field optical coherence tomography.* J Biomed Opt, 2007. **12**(6): p. 064024.

67. Kaluzny, B.J., et al., *Spectral optical coherence tomography in video-rate and 3D imaging of contact lens wear.* Optom Vis Sci, 2007. **84**(12): p. 1104-9.

68. Hidalgo-Aguirre, M., et al., *Automatic segmentation of the optic nerve head for deformation measurements in video rate optical coherence tomography.* J Biomed Opt, 2015. **20**(11): p. 116008.

69. Hendel, T., et al., *Fluorescence changes of genetic calcium indicators and OGB-1 correlated with neural activity and calcium in vivo and in vitro.* J Neurosci, 2008. **28**(29): p. 7399-411.

70. Holekamp, T.F., D. Turaga, and T.E. Holy, *Fast three-dimensional fluorescence imaging of activity in neural populations by objective-coupled planar illumination microscopy.* Neuron, 2008. **57**(5): p. 661-72.

71. Hayashi, Y., et al., *Spatio-temporal control of neural activity in vivo using fluorescence microendoscopy.* Eur J Neurosci, 2012. **36**(6): p. 2722-32.

72. Sinha, S., et al., *High-speed laser microsurgery of alert fruit flies for fluorescence imaging of neural activity.* Proc Natl Acad Sci U S A, 2013. **110**(46): p. 18374-9.

73. Friman, O., et al., *Detection of neural activity in fMRI using maximum correlation modeling.* Neuroimage, 2002. **15**(2): p. 386-95.

74. Chevrier, A., M.D. Noseworthy, and R. Schachar, *Neural activity associated with failed inhibition: an event related fMRI study or performance monitoring.* Brain Cogn, 2004. **54**(2): p. 163-5.

75. Lee, T.M., et al., *Neural activity associated with cognitive regulation in heroin users: A fMRI study.* Neurosci Lett, 2005. **382**(3): p. 211-6.

76. Olson, I.R., et al., *Using perfusion fMRI to measure continuous changes in neural activity with learning.* Brain Cogn, 2006. **60**(3): p. 262-71.

77. Ekstrom, A., *How and when the fMRI BOLD signal relates to underlying neural activity: the danger in dissociation.* Brain Res Rev, 2010. **62**(2): p. 233-44.

78. Ohye, C., et al., *Stereotactic CT scan and its correlation with the neural activity of deep structures.* Appl Neurophysiol, 1980. **43**(3-5): p. 183-8.

79. Tagamets, M.A. and B. Horwitz, *Interpreting PET and fMRI measures of functional neural activity: the effects of synaptic inhibition on cortical activation in human imaging studies.* Brain Res Bull, 2001. **54**(3): p. 267-73.

80. Horwitz, B., *Relating fMRI and PET signals to neural activity by means of large-scale neural models.* Neuroinformatics, 2004. **2**(2): p. 251-66.

81. Lockwood, A.H., et al., *Multi-site phasic neural activity mediates the execution of an auditory continuous performance task: a PET and electrophysiological study.* J Neuroimaging, 2008. **18**(4): p. 364-74.

82. Jimbo, Y., *Recording neural activity by electrode-array substrates.* Electrochemistry, 1999. **67**(3): p. 276-279.

83. Jayaraman, V. and G. Laurent, *Evaluating a genetically encoded optical sensor of neural activity using electrophysiology in intact adult fruit flies.* Front Neural Circuits, 2007. **1**: p. 3.

84. Panetsos, F. and C. Avendano, *Neural activity of the Central Nervous System after long-term implants of sieve-electrodes to the peripheral nerves.* 2007 3rd International Ieee/Embs Conference on Neural Engineering, Vols 1 and 2, 2007: p. 44-+.

85. Shew, W.L., T. Bellay, and D. Plenz, *Simultaneous multi-electrode array recording and two-photon calcium imaging of neural activity.* Journal of Neuroscience Methods, 2010. **192**(1): p. 75-82.

86. Gage, G.J., et al., *Surgical Implantation of Chronic Neural Electrodes for Recording Single Unit Activity and Electrocorticographic Signals.* Jove-Journal of Visualized Experiments, 2012(60).

87. Kondo, Y., et al., *Temporal relation between neural activity and neurite pruning on a numerical model and a microchannel device with micro electrode array.* Biochemical and Biophysical Research Communications, 2017. **486**(2): p. 539-544.

88. Yang, J., et al., *Fast multispectral diffuse optical tomography system for in vivo three-dimensional imaging of seizure dynamics.* Appl Opt, 2012. **51**(16): p. 3461-9.

89. Zhang, T., et al., *Pre-seizure state identified by diffuse optical tomography.* Sci Rep, 2014. **4**: p. 3798.

90. Chen, J.W., A.M. O'Farrell, and A.W. Toga, *Optical intrinsic signal imaging in a rodent seizure model.* Neurology, 2000. **55**(2): p. 312-5.

91. Lu, R.W., Q.X. Zhang, and X.C. Yao, *Circular polarization intrinsic optical signal recording of stimulus-evoked neural activity.* Opt Lett, 2011. **36**(10): p. 1866-8.

92. Liu, W., et al., *OCT-Angiography for Non-Invasive Monitoring of Neuronal and Vascular Structure in Mouse Retina: Implication for Characterization of Retinal Neurovascular Coupling.* EC Ophthalmol, 2017. **5**(3): p. 89-98.

93. Bodenschatz, N., et al., *Detecting structural information of scatterers using spatial frequency domain imaging.* J Biomed Opt, 2015. **20**(11): p. 116006.

94. Singh-Moon, R.P., et al., *Spatial mapping of drug delivery to brain tissue using hyperspectral spatial frequency-domain imaging.* J Biomed Opt, 2014. **19**(9): p. 96003.

95. Lazebnik, M., et al., *Functional optical coherence tomography for detecting neural activity through scattering changes.* Opt Lett, 2003. **28**(14): p. 1218-20.

96. Yao, X.C., et al., *Rapid optical coherence tomography and recording functional scattering changes from activated frog retina.* Appl Opt, 2005. **44**(11): p. 2019-23.

97. Graf, B.W., et al., *Detecting intrinsic scattering changes correlated to neuron action potentials using optical coherence imaging.* Opt Express, 2009. **17**(16): p. 13447-57.

98. Yeh, Y.J., et al., *Optical coherence tomography for cross-sectional imaging of neural activity.* Neurophotonics, 2015. **2**(3): p. 035001.

99. Akkin, T., et al., *Detection of neural activity using phase-sensitive optical low-coherence reflectometry.* Opt Express, 2004. **12**(11): p. 2377-86.

100. Akkin, T., C. Joo, and J.F. de Boer, *Depth-resolved measurement of transient structural changes during action potential propagation.* Biophys J, 2007. **93**(4): p. 1347-53.

101. Chen, Y., et al., *Optical coherence tomography (OCT) reveals depth-resolved dynamics during functional brain activation.* J Neurosci Methods, 2009. **178**(1): p. 162-73.

102. Akkin, T., D. Landowne, and A. Sivaprakasam, *Detection of Neural Action Potentials Using Optical Coherence Tomography: Intensity and Phase Measurements with and without Dyes.* Front Neuroenergetics, 2010. **2**.

103. Tong, M.Q., et al., *OCT intensity and phase fluctuations correlated with activity-dependent neuronal calcium dynamics in the Drosophila CNS [Invited]*. Biomedical Optics Express, 2017. **8**(2): p. 726-735.

104. Bizheva, K., et al., *Imaging ex vivo healthy and pathological human brain tissue with ultra-high-resolution optical coherence tomography.* J Biomed Opt, 2005. **10**(1): p. 11006.

105. Bohringer, H.J., et al., *Time-domain and spectral-domain optical coherence tomography in the analysis of brain tumor tissue.* Lasers Surg Med, 2006. **38**(6): p. 588-97.

106. Osiac, E., et al., *Optical coherence tomography as a promising imaging tool for brain investigations.* Rom J Morphol Embryol, 2014. **55**(2 Suppl): p. 507-12.

107. Kut, C., et al., *Detection of human brain cancer infiltration ex vivo and in vivo using quantitative optical coherence tomography.* Sci Transl Med, 2015. **7**(292): p. 292ra100.

108. Cardenas, D.P., et al., *Functional MRI during hyperbaric oxygen: Effects of oxygen on neurovascular coupling and BOLD fMRI signals.* Neuroimage, 2015. **119**: p. 382-9.

109. Blicher, J.U., et al., *Visualization of altered neurovascular coupling in chronic stroke patients using multimodal functional MRI.* J Cereb Blood Flow Metab, 2012. **32**(11): p. 2044-54.

110. Sander, C.Y., et al., *Neurovascular coupling to D2/D3 dopamine receptor occupancy using simultaneous PET/functional MRI.* Proc Natl Acad Sci U S A, 2013. **110**(27): p. 11169-74.

111. Akerboom, J., et al., *Optimization of a GCaMP calcium indicator for neural activity imaging.* J Neurosci, 2012. **32**(40): p. 13819-40.

112. Blasdel, G.G. and G. Salama, *Voltage-sensitive dyes reveal a modular organization in monkey striate cortex.* Nature, 1986. **321**(6070): p. 579-85.

113. Fromherz, P. and C.O. Muller, *Voltage-sensitive fluorescence of amphiphilic hemicyanine dyes in neuron membrane.* Biochim Biophys Acta, 1993. **1150**(2): p. 111-22.

114. Homma, R., et al., *Wide-field and two-photon imaging of brain activity with voltage- and calcium-sensitive dyes.* Philosophical Transactions of the Royal Society B-Biological Sciences, 2009. **364**(1529): p. 2453-2467.

115. Yang, H., et al., *In vivo imaging of epileptic foci in rats using a miniature probe integrating diffuse optical tomography and electroencephalographic source localization.* Epilepsia, 2015. **56**(1): p. 94-100.

116. Bahar, S., et al., *Intrinsic optical signal imaging of neocortical seizures: the 'epileptic dip'.* Neuroreport, 2006. **17**(5): p. 499-503.

117. Chen, J.W.Y. and A.W. Toga, *Optical intrinsic signal imaging of acute neocortical seizures in rats.* Epilepsia, 2005. **46**: p. 202-202.

118. Schwartz, T.H. and T. Bonhoeffer, *In vivo optical mapping of epileptic foci and surround inhibition in ferret cerebral cortex.* Nature Medicine, 2001. **7**(9): p. 1063-1067.

119. Rajagopalan, U.M. and M. Tanifuji, *Functional optical coherence tomography reveals localized layer-specific activations in cat primary visual cortex in vivo.* Optics Letters, 2007. **32**(17): p. 2614-2616.

120. Tian, L., et al., *Imaging neural activity in worms, flies and mice with improved GCaMP calcium indicators.* Nat Methods, 2009. **6**(12): p. 875-81.

121. Han, Z., et al., *Mechanistic studies of the genetically encoded fluorescent protein voltage probe ArcLight.* PLoS One, 2014. **9**(11): p. e113873.

122. Prati, F., et al., *Intracoronary optical coherence tomography, basic theory and image acquisition techniques.* Int J Cardiovasc Imaging, 2011. **27**(2): p. 251-8.

123. Huang, J., et al., *Measurement of a multi-layered tear film phantom using optical coherence tomography and statistical decision theory.* Biomed Opt Express, 2014. **5**(12): p. 4374-86.

124. Curatolo, A., B.F. Kennedy, and D.D. Sampson, *Structured three-dimensional optical phantom for optical coherence tomography.* Opt Express, 2011. **19**(20): p. 19480-5.

125. Cohen, L.B., R.D. Keynes, and B. Hille, *Light scattering and birefringence changes during nerve activity.* Nature, 1968. **218**(5140): p. 438-41.

126. Akkin, T., D. Landowne, and A. Sivaprakasam, *Detection of Neural Action Potentials Using Optical Coherence Tomography: Intensity and Phase Measurements with and without Dyes.* Frontiers in Neuroenergetics, 2010. **2**: p. 22.

127. Iwasa, K., I. Tasaki, and R.C. Gibbons, *Swelling of nerve fibers associated with action potentials.* Science, 1980. **210**(4467): p. 338-9.

128. Andrew, R.D. and B.A. MacVicar, *Imaging cell volume changes and neuronal excitation in the hippocampal slice.* Neuroscience, 1994. **62**(2): p. 371-83.

129. Fang-Yen, C.M., et al. *Neural interferometry: first non-contact measurements of action potential-induced nerve swelling*. in *Biomedical Topical Meeting*. 2004. Miami Beach, Florida: Optical Society of America.

130. Tasaki, I., et al., *Changes in fluorescence, turbidity, and birefringence associated with nerve excitation.* Proc Natl Acad Sci U S A, 1968. **61**(3): p. 883-8.

131. Cohen, L.B., *Changes in neuron structure during action potential propagation and synaptic transmission.* Physiol Rev, 1973. **53**(2): p. 373-418.

132. Akkin, T., D. Landowne, and A. Sivaprakasam, *Optical coherence tomography phase measurement of transient changes in squid giant axons during activity.* J Membr Biol, 2009. **231**(1): p. 35-46.

133. Nunnemacher, R.F. and P.P. Davis, *The fine structure of the limulus optic nerve.* J Morphol, 1968. **125**(1): p. 61-70.

134. Hodgkiss, J.P. and H.M. McIlroy, *The conduction velocity, number, and diameter of unmyelinated fibers in Remak's nerve.* Experientia, 1985. **41**(7): p. 919-21.

135. Pollak, V.A., et al., *Non-invasive determination of the distribution of the conduction velocity of the large-diameter fibers in peripheral nerves. Estimate based upon a single recording of the stimulus response of the nerve.* Med Prog Technol, 1992. **18**(4): p. 217-25.

136. Campbell, C.E., et al., *The transcription factor Nfix is essential for normal brain development.* BMC Dev Biol, 2008. **8**: p. 52.

137. Park, B.H., et al., *Real-time fiber-based multi-functional spectral-domain optical coherence tomography at 1.3 mu m.* Optics Express, 2005. **13**(11): p. 3931-3944.